Detection of Copper by the ChemCam Instrument Along Curiosity's Traverse in Gale Crater, Mars: Elevated Abundances in Glen Torridon

Walter Goetz, Erwin Dehouck, Patrick Gasda, Jeffrey Johnson, Pierre-Yves Meslin, Nina Lanza, Roger Wiens, William Rapin, Jens Frydenvang, Valerie Payré, et al.

JGR Planets

RESEARCH ARTICLE
10.1029/2021JE007101

Special Section:
The Curiosity rover's investigation of Glen Torridon and the surrounding area

Detection of Copper by the ChemCam Instrument Along Curiosity's Traverse in Gale Crater, Mars: Elevated Abundances in Glen Torridon

Walter Goetz[1,2], Erwin Dehouck[3], Patrick J. Gasda[4], Jeffrey R. Johnson[5], Pierre-Yves Meslin[6], Nina L. Lanza[4], Roger C. Wiens[7], William Rapin[6], Jens Frydenvang[8], Valerie Payré[9], and Olivier Gasnault[6]

[1]Max Planck Institute for Solar System Research (MPS), Göttingen, Germany, [2]Geoscience Center, Department of Geobiology, Georg-August-Universität Göttingen, Göttingen, Germany, [3]Université de Lyon, UCBL, ENSL, UJM, CNRS, LGL-TPE, Villeurbanne, France, [4]Los Alamos National Laboratory (LANL), Los Alamos, NM, USA, [5]Johns Hopkins University, Applied Physics Laboratory, Laurel, MD, USA, [6]Institut de Recherche en Astrophysique et Planetologie (IRAP), Toulouse, France, [7]Earth, Atmospheric, and Planetary Sciences, Purdue University, West Lafayette, IN, USA, [8]University of Copenhagen, Copenhagen, Denmark, [9]Northern Arizona University, Flagstaff, AZ, USA

Abstract Laser-induced breakdown spectroscopy, as utilized by the ChemCam instrument onboard the Curiosity rover, detected enhanced abundances of the element copper. Since landing in Gale crater (6 August 2012), 10 enhancements in copper abundance were observed during 3007 Martian days (sols) of rover operations and 24 km of driving (as of 20 January 2021). The most prominent ones were found in the Kimberley area on the crater floor (Aeolis Palus) and in Glen Torridon (GT) on the lower flanks of Aeolis Mons (Mt. Sharp). Enhancements in copper record the former existence of modestly acidic and oxidizing fluids, which were more oxidizing in Kimberley than in GT. Of the two main types of bedrock in the lowest part of GT, Mg-rich "coherent" and K-rich "rubbly" (named based on their outcrop expression), copper was detected only in coherent, not in rubbly bedrock. The difference between these two types of bedrock may be due to difference in provenance. Alternatively, based on a recently developed lacustrine-groundwater mixing model, we suggest that rubbly bedrock was altered by modestly acidic, shallow-subsurface lake water that leached out both copper and manganese, while coherent bedrock was affected by dominantly alkaline fluids which would be consistent with its mineralogical composition (including siderite) as returned by the CheMin instrument onboard the rover. Higher up in GT, ChemCam data indicated significant gradients in the copper concentration in coherent bedrock on a local scale of only a few meters, which suggests a different alteration style and possibly different types of diagenetic fluids.

Plain Language Summary Gale crater, Mars, about 152-km in diameter and 3.6 Ga in age, has a central mound that is partly of sedimentary origin. To date (July 2022), the NASA rover Curiosity has been exploring the crater floor and the lower-most 600 m (in elevation) of sediments of that mound. ChemCam, an instrument mounted on top of the remote-sensing mast utilizing Laser-Induced Breakdown Spectroscopy, has been measuring chemical composition and specifically copper abundances along the rover traverse. We identified 10 areas of copper enhancement along Curiosity's traverse. In the Kimberley formation on the crater floor, copper was identified in a manganese-rich sandstone. Later on, some 350 m above Kimberley, high copper abundances were detected in magnesium-rich mudstone and in iron-rich sandstone in the Jura and Knockfarril Hill member, respectively. Following earlier work about copper in Gale crater (Payré et al., 2019, https://doi.org/10.1016/j.icarus.2018.12.015), we postulate a copper-rich source region north of Gale crater and suggest that copper-rich detrital material delivered to these areas in Gale crater. Taking into account the chemical and mineralogical composition of these types of bedrock, we conclude that copper was mobilized by later acidic and oxidizing fluids.

Key Points:

- High copper abundances (200–400 ppm) are found in specific areas along the rover traverse
- In the Jura member in Glen Torridon (GT), copper is detected only in coherent bedrock, not in rubbly bedrock
- In the Knockfarril Hill member in GT, there is evidence for the redistribution of copper and iron by acidic, oxidizing fluids

Supporting Information:

Supporting Information may be found in the online version of this article.

Correspondence to:
W. Goetz,
walter.goetz@mail.de

Citation:
Goetz, W., Dehouck, E., Gasda, P. J., Johnson, J. R., Meslin, P.-Y., Lanza, N. L., et al. (2023). Detection of copper by the ChemCam instrument along Curiosity's traverse in Gale crater, Mars: Elevated abundances in Glen Torridon. *Journal of Geophysical Research: Planets*, *128*, e2021JE007101. https://doi.org/10.1029/2021JE007101

Received 18 OCT 2021
Accepted 15 DEC 2022

Author Contributions:
Conceptualization: Walter Goetz, Erwin Dehouck, Patrick J. Gasda
Data curation: Erwin Dehouck, Jeffrey R. Johnson, Pierre-Yves Meslin
Formal analysis: Patrick J. Gasda
Investigation: Patrick J. Gasda, Jeffrey R. Johnson, Pierre-Yves Meslin

1. Introduction

NASA's Curiosity rover has been exploring the floor of Gale crater and the lower flanks of its sedimentary central mound, Mt. Sharp (officially named Aeolis Mons), since August 2012. The science payload includes the ChemCam (Chemistry and Camera) instrument suite (Maurice et al., 2012; Wiens et al., 2012) that is mounted on top of the rover's remote sensing mast. ChemCam uses Laser-Induced Breakdown Spectroscopy (LIBS) to track

Methodology: Walter Goetz, Erwin Dehouck, Patrick J. Gasda, Nina L. Lanza, Roger C. Wiens, William Rapin, Jens Frydenvang, Valerie Payré, Olivier Gasnault
Software: Walter Goetz
Validation: Erwin Dehouck, Patrick J. Gasda
Visualization: Walter Goetz
Writing – original draft: Walter Goetz

the chemical evolution of Martian surface materials along the traverse and up to 7 m away from the rover. This article describes the detection of the element copper (Cu) along the rover traverse with a focus on the Kimberley area and the recently explored clay-mineral rich area *Glen Torridon* (GT). So far, Martian Cu has been found in a specific outcrop in Gusev crater (Clark et al., 2007) and in different types of surface material (including bedrock, float rocks, and diagenetic features) and different geologic areas in Gale crater. The enrichment of Cu in Martian bedrock provides constraints on the diagenetic history of that bedrock. It may also be relevant to the astrobiological exploration of Mars since Cu has been identified as a potentially important trace element for the origin of life on Earth (Patel et al., 2015).

2. Background

2.1. Copper on Earth and Mars

Cu occurs naturally in the oxidation states (0), (+1), or (+2), the latter being dominant in aqueous solution. In the context of magmatic fractionation, Cu behaves as an incompatible element, unless the magma is saturated in sulfide (Jenner et al., 2010; Park et al., 2013, 2015). The terrestrial crust contains on average 68 ppm Cu (typically ∼100 ppm in mafic rocks and ∼10 ppm in felsic rocks, Ure & Berrow, 1982; Pohl, 2011). A significant fraction of crustal Cu is incorporated in common rock-forming minerals such as pyroxene, olivine, biotite, amphibole, magnetite, and plagioclase, typically in the 60–120 ppm range, with plagioclases usually ranging at the lower end of this interval (Ure & Berrow, 1982; see also Core et al., 2005). The remainder is concentrated in Cu ore deposits. The prospects of finding Cu on Mars are lower than on Earth: Cu abundances in Martian meteorites generally do not exceed 30 ppm and are generally in the range 3–20 ppm (Udry et al., 2020). In fact, out of 94 Martian meteorites (as compiled by Udry et al. (2020)), only three meteorites contained more than 30 ppm Cu, that is, the shergottites NWA 6234 (41 ppm), EETA 79001A (73 ppm), and NWA 11043 (842 ppm). Excluding the last mentioned (i.e., NWA 11043), the remaining 93 meteorites contained an average of 11.1 ppm Cu (standard deviation: 8.9 ppm). Furthermore, due to low pressure inside Mars (as compared to Earth), Cu behaved as a more strongly siderophile element and was therefore preferentially concentrated in the Martian core (Payré et al., 2019; Wang & Becker, 2017). Accordingly, Cu abundances in the Martian mantle are estimated to be in the range 2–5 ppm (Lodders & Fegley, 1997; Payré et al., 2019; Taylor, 2013; Yoshizaki & McDonough, 2020).

Most Cu enrichments on Earth can be explained by the dissolution and transport of Cu^{2+} by acidic, oxidizing fluids followed by sudden precipitation in the presence of sulfide anions (Pohl, 2011). However, there is a second way to enrich Cu, namely by scavenging Cu^{2+} ions from solution by adsorption. The following examples of adsorbing compounds are listed in order of decreasing adsorption efficiency: manganese oxides > organic matter > iron oxides > clay minerals (Bradl, 2004; Ure & Berrow, 1982). Typically, Cu adsorption is strongest at pH > 6 and remains strong in the basic range (Bradl, 2004). In particular, Cu^{2+} can be removed from the solution by precipitation of Mn(II)- and/or Fe(III) oxides. Initially, these phases may be amorphous or crystalline. However, over geologic time, amorphous phases may become crystalline, for example, pyrolusite (MnO_2) or hematite, with the latter phase being a frequently detected minor mineral in GT (Thorpe et al., 2022).

There are at least two mechanisms by which Cu may enter a mineral structure: (a) substitution of Fe^{2+} by Cu^{2+} (owing to their similar ionic radii), as demonstrated for magnetite (Core et al., 2005), and (b) in the form of sulfide melt inclusions in silicate minerals (pyroxenes, amphiboles, and plagioclases) or quartz (Audetat et al., 2018; Halter et al., 2005). Alexander and Thomas (2011) reported about enriched Cu in Deccan basalts (typically 100–200 ppm, although in some places up to 500 ppm). According to these authors, Cu is associated with titanomagnetite in these basalts, but it remains unclear whether Cu ions are part of the crystal lattice or Cu sulfide inclusions.

Although Cu is often at or below the limits of detection and quantification for recent Mars rovers, some compelling observations of enhanced Cu have been made: 230 ppm Cu was reported in the Independence outcrop, Gusev crater (Clark et al., 2007) and typically a few hundred ppm of Cu (locally up to 1,100 ppm) was detected using the APXS (Gellert et al., 2014; VanBommel et al., 2019) and ChemCam instruments (Goetz et al., 2016, 2017, 2018, 2019, 2020; Payré et al., 2019) at various places in Gale crater. Payré et al. (2019) postulated the existence of a hydrothermal Cu deposit nearby and outside Gale crater, possibly not far beyond its northern crater wall. This could be a porphyry Cu deposit or a deposit generated by impact or fumarolic activity. According to Payré et al. (2019), Cu-rich clasts would have been transported to the *Kimberley* area on the crater floor in the *Bradbury*

group of the stratigraphic column explored during Sols 574–632 (Fedo et al., 2022; Grotzinger et al., 2015; Rice et al., 2017; Vasavada, 2022).

One of the main goals of NASA's Curiosity rover is to characterize the depositional environment of Gale sediments and assess its habitability (Vasavada, 2022). In the context of these investigations as well as Mars Sample Return, a major campaign kicked off by the Mars-2020 rover *Perseverance*, it is worth mentioning that Cu has become an element of astrobiological interest, as it may serve as a potential catalyst for prebiotic self-assemblage of molecular building blocks of life (Clark et al., 2021). Indeed, Patel et al. (2015) and Sutherland (2015) have developed a mechanism for "Cu- and UV-supported reductive homologation of hydrogen cyanide, HCN", that is, the generation of carbon chains of any length, starting from HCN, a molecule that has been tentatively detected by Evolved Gas Analysis by the SAM instrument (Stern et al., 2014, 2015). HCN can be formed by the reaction between meteoritic carbon (atomized during impact) and atmospheric nitrogen (Ferus et al., 2017; Patel et al., 2015; Sasselov et al., 2020). It is an excellent starting molecule for the generation of simple prebiotic organic molecules as it contains H, C, and N, three chemical elements essential for life, in a nearly ideal ratio. These studies show that Cu may have been a key element in the transition from a prebiotic environment to earliest forms of life. It is therefore of interest to assess Cu abundance on Mars, particularly on the floor of Gale crater and the lower flanks of Mt. Sharp, that is, Curiosity's working area. A critical aspect of the above described prebiotic chemical pathway may be the low availability of copper in either Earth's or Mars' crust. Therefore, Xu et al. (2018) have been developing an alternative model that proposes to replace the redox couple of Cu(I)/Cu(II) by Fe(II)/Fe(III). The latter is not as efficient as the former, but strengthens the prebiotic model by invoking a major element on the surface of Mars.

2.2. The Curiosity Rover Mission Up to Sol 3007

After landing in Gale crater in August 2012, the rover drove eastward into a shallow basin named Yellowknife Bay (YB). Thereafter, it continued its traverse throughout the Bradbury area in a broadly southwestern direction. Important waypoints during that traverse were the Kimberley formation (mostly sandstone) and the Pahrump Hills (PHm) mudstone (Figures S1a–S1e in Supporting Information S1). After detailed exploration of the PHm, the rover started its ascent of Mt. Sharp. About 300 m above PHm campaigns were conducted at Vera Rubin ridge (VRR; Sols 1800–2300) and GT (Sols 2300–3070, Figure S1f in Supporting Information S1). The latter campaign included the detailed exploration of the Jura member (Jm), the overlying Knockfarril Hill member (KHm), and the Glasgow member (Gm) that overlies KHm. We distinguish between the part of the Jm that belongs to the VRR and the one in GT, denoted as Jm/VRR and Jm/GT, respectively (Bennett et al., 2022; Fedo et al., 2022). Finally, the Gm is overlain by the Stimson formation (Sf) that is not part of GT. A portion of the Sf was explored during Sols 2695–2732, approximately in the middle of the GT campaign. The Gm is separated from the Sf by a major unconformity that is called the Siccar Point (SP) unconformity. The Sf appears to be an eolian sandstone (Banham et al., 2018, 2021, 2022; Bedford, Schwenzer, et al., 2019; Bedford et al., 2020) as opposed to the older GT members that have been interpreted as various flavors of past fluvial/lacustrine environments (Bennett et al., 2022; Caravaca et al., 2022; Fedo et al., 2022; Gasda et al., 2022). Vasavada (2022) and Bennett et al. (2022) provided a detailed mission report (including report on major science results) for Sols 0–2900 and 2300–3070, respectively. We present here an overview of relevant morphologic features, lithologies, outcrops, and targets.

VRR is a ~200 m wide, NE-SW striking ridge with a pronounced hematite signature in orbital data. Around Sol 2300, the rover descended into a shallow trough that is referred to as Jm/GT or the smooth-ridged Clay-Bearing Unit (CBU) since this unit has a particularly clear and continuous spectral signature of clay minerals as observed from orbit (Bennett et al., 2022). In that trough, two different types of bedrock were recognized based on their visual appearance and compositional data (e.g., Dehouck et al., 2022): (a) "coherent bedrock" that is constrained to isolated areas and (b) "rubbly bedrock" that covers large areas and is the dominating type of bedrock in Jm/GT. Coherent bedrock was characterized by two drill campaigns in the Aberlady (AB; Sol 2365–2370) and Kilmarie (KM; Sol 2380–2390) regions. From Sol 2440 onward and moving further into KHm, the rover encountered increasingly greater exposures of coherent bedrock. Caravaca et al. (2022) observed that rubbly bedrock is the typical bedrock facies in Jm/GT, while coherent bedrock is more typical of KHm. The rover conducted two major science campaigns in KHm: one at the outcrop Glen Etive (GE; Sol 2480–2550) and one at Mary Anning (MA; Sol 2830–2920). The latter campaign included three drill campaigns, referred to as "MA", "MA 3", and "Groken"

(Bennett et al., 2022). The Groken drill campaign was conducted near the southeastern edge of the MA outcrop (Figure S5 in Supporting Information S1) and near the ChemCam and APXS *Ayton* targets (ChemCam: Ayton, Ayton 2, and Ayton 2 dp [deep profile]; APXS: Ayton raster 1 to 3). An important result of this campaign was the detection of elevated Mn and P in the nodules in Ayton's nodule-rich layers (see Figure 7 in Gasda et al. (2022)). Finally, the MA science campaign also included the exploration of the so-called "Dark Strata" (DS; also referred to as "dark-toned strata", Gasda et al. (2022)), another outcrop that was a few meters west of MA that is discussed further below.

On Sol 3007, the ChemCam instrument experienced an anomaly that precluded LIBS measurements until they resumed from Sol 3107. Therefore, the present manuscript ends at Sol 3007, although the exploration of GT continued through Sol ~3072, when the rover gradually transitioned into the magnesium sulfate-bearing strata that overlie GT (Bennett et al., 2022).

3. Data and Methods

The ChemCam instrument onboard Curiosity (Maurice et al., 2012; Wiens et al., 2012) utilizes LIBS to determine abundances for major element oxides (SiO_2, TiO_2, Al_2O_3, FeOT, MgO, CaO, Na_2O, K_2O, and MnO; Clegg et al., 2017; Gasda et al., 2021; Wiens et al., 2013) and for some trace elements (Li, Rb, Sr, and Ba; Ollila et al., 2014; Payré et al., 2017). At each point on the Martian surface that is sampled by the ChemCam laser (λ = 1,067 nm), the spectrum of light emitted by the laser-generated plasma cloud is recorded by detectors in the ultraviolet, violet, and visible/near-infrared regions (from here on referred to, respectively, as UV, VIO, and VNIR). Radiance data acquired without laser action can be converted into relative reflectance spectra that are referred to as "ChemCam passive spectra" and provide additional information on the LIBS-analyzed targets (Johnson et al., 2015). Besides the LIBS-related modules, the ChemCam instrument suite includes the Remote Micro-Imager (RMI) that provides high-resolution (gray-scale) images of the LIBS-analyzed targets (Le Mouelic et al., 2015).

Cu has 2 major emission lines, centered respectively at λ = 324.789 and 327.428 nm (according to the current ChemCam wavelength calibrated to vacuum, Clegg et al., 2017; Wiens et al., 2013). Each Cu line overlaps strongly with three other (mostly titanium) emission lines, resulting in the presence of two broad emission bands. From here on, these two lines/bands are referred to as "Cu324" and "Cu327" or as "left band" and "right band", respectively.

Prior to the analysis of these bands, the spectra were normalized to the spectral total in the VNIR spectrum. Among the different models for normalization (Fabre et al., 2014; Ollila et al., 2014), the VNIR normalization (also applied to quantification of boron, Gasda et al., 2017) provided the most consistent data set in the present case of Cu analysis.

The deconvolution of the Cu/Ti emission bands largely followed the procedure described earlier by Payré et al. (2019) and Goetz et al. (2020) (see Table S1 in Supporting Information S1 for peak fitting constraints). Figure 1 demonstrates peak fitting using the example of target "Crail", one of the most prominent Cu-bearing targets in the Jura member (Jm/GT). A weak Fe line, located very close to Cu324, leads to an overestimation of the Cu324 peak areas for samples that are rich in Fe. For this reason, two approaches were used in this work: (a) explore the geochemical properties of Cu-bearing surface material, especially bedrock, without considering the computed relative abundance that might be affected by Fe and (b) compare inferred Cu abundances to those of other elements (Mg, K, Fe, and Mn in particular). Further improvement of data analysis, especially in multi-peak fitting and fit constraints, will likely decrease Cu's limit of detection (LOD) and increase the number of Cu-bearing targets in Gale crater.

In the context of this work, "Cu-bearing points" are those that contain Cu above ChemCam's LOD, which is ~50–100 ppm, depending on the presence of emission lines from other elements (the limit of quantification [LOQ] is ~200 ppm (Payré et al., 2019), again depending on the presence of other elements). In most ChemCam spectra, no Cu is detected. This indicates that (a) ChemCam's detection limit for Cu is not particularly low in comparison to standard laboratory techniques and (b) a target where Cu is detected by ChemCam may be termed "Cu enriched Figure 2 plots the Cu327 areas for all Cu-bearing points in the sol range 0–3007 as a function of elevation. In addition, the running average of these areas was computed within 7.5-m wide elevation intervals, scaled up by an arbitrary factor (i.e., a factor of 3.2) and plotted as a thick red line in Figure 2. Whenever that

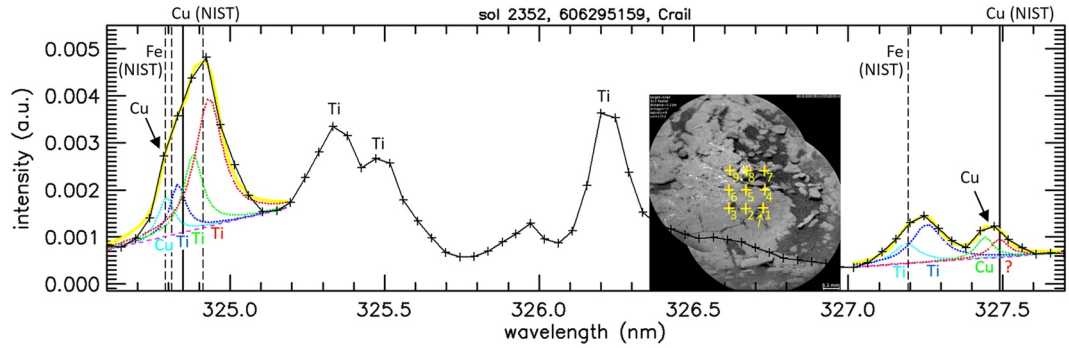

Figure 1. Demonstration of Cu peak fitting for the target "Crail", point #1. Both Cu bands have been fitted by four overlapping Lorentzian functions. In both cases, the "partial Lorentzians" are cyan, blue, green, and red (in that sequence) dotted lines. The sum of these four Lorentzians is drawn as a thick, solid yellow line. In the left band, the Cu line is the cyan curve (i.e., the left-most with $\lambda \sim 324.8$ nm), in the right band, the Cu line is the green curve ($\lambda \sim 327.5$ nm). Prominent Cu features in the spectrum are additionally marked by two thick black arrows. Vertical lines mark the wavelengths (in the vacuum) for Cu (thick black lines) and Fe (red dashed lines) as provided by the NIST Atomic Spectra Database. In this spectral area (near the long-wavelength end of ChemCam's UV detector), the ChemCam wavelength calibration is off (short) by ~0.04 nm (note the spectral distance between one of the black arrows and the nearby solid black (vertical) line marking the NIST wavelength). The inset shows the ChemCam-Remote Micro-Imager image of Crail (sol 2352, ccam04352) with the locations of all ChemCam laser-induced breakdown spectroscopy points (yellow plus signs). The spectrum shown in this figure was acquired on ChemCam point #1 (marked by a yellow arrow). All ChemCam points except #8 were found to be enriched in Cu.

scaled running average exceeded a threshold of 3 10^{-5}, the corresponding cluster of Cu-bearing ChemCam points was interpreted to represent a "region of enhanced Cu abundance".

The data analysis presented in this manuscript covers all types of surface material, including bedrock, float rocks, and diagenetic features although some focus is on bedrock. Only ChemCam data of "good quality" were taken into account. The standard checks used to validate ChemCam LIBS data for archiving in the Planetary Data System were used. These include thresholds for total optical emission, distance, and checks on the focus quality.

We have identified ~360 Cu-enriched ChemCam points (~120 in the GT area). The associated peak areas (Cu324 and Cu327) were plotted against each other and fitted by a straight line with slope 0.996 and correlation coefficient $R^2 = 0.61$ (Figure S2 in Supporting Information S1). Based on the NIST Atomic spectra data base (Kramida & Ralchenko, 1999), a slope of ~1 is expected, since both Cu I emission lines listed in that database have similar relative strength.

Of particular importance for this work are ChemCam's major element oxide predictions (below referred to as MOC [Major Oxide Composition] data). In this work, the latest calibration for MOCs includes a distance correction for SiO_2, Al_2O_3, Na_2O, and K_2O (Wiens et al., 2021). The sums of major oxides (usually referred to as "totals") are of particular importance as they are a proxy for missing compounds, that is, compounds that are not currently quantified by the routine ChemCam data processing pipeline (Clegg et al., 2017). In this study, it was noted that the Cu324 and Cu327 peak areas are not consistent with each other for ChemCam points with totals <50 wt%, that is, the Cu324 area remains close to zero independent of the corresponding Cu327 area. This implies that these points are actually *not* enriched in Cu. Therefore, ChemCam points with totals <50 wt% were discarded from the present study.

All data tables in this manuscript are sorted according to stratigraphic sequence. There is some (limited) overlap between different data tables in this manuscript in order to demonstrate how they are linked to each other. An effort has been made to ensure consistency with similar data tables and results in Dehouck et al. (2022).

Finally, a note on the term "bedrock" as it will be used in this manuscript: Following Dehouck et al. (2022), we require (a) that a ChemCam point is identified as "bedrock" by visual inspection, as based on all images available for that specific ChemCam point (RMI, MCAM, and NCAM) and (b) that CaO <5 wt% *OR* Totals >95 wt%. This enables the removal of calcium-sulfate contribution from the geochemical signature of some bedrock, given that calcium-sulfate veins may be very late additions to the original bedrock. The procedure is based on the assumption that even submicroscopic veins that would not be visible in the images could still be noticed in the

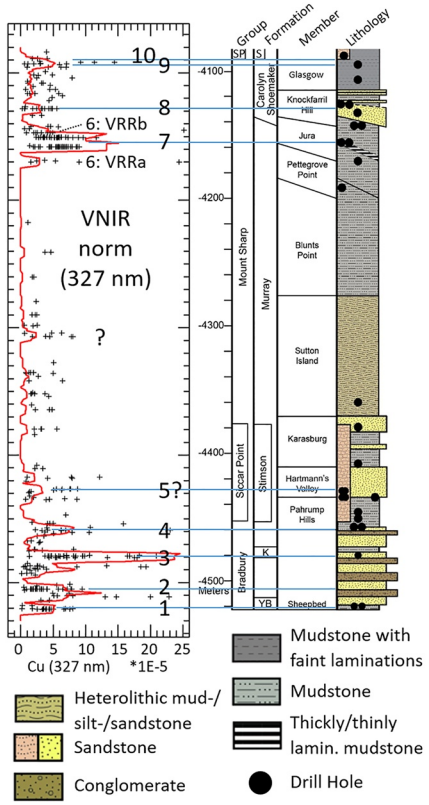

Label	Formation (f) or Member (m) (Cu pts.)	Prominent targets	Lithology	Sol	Elevation (max/min)	Cu (ppm) (std. error)
10	Stimson (Sf, 10x)	Glen Finglas 2	sandstone	2693-2733	-4091 -4093	197 (45)
9	Glasgow (Gm, 24x)	Cheviot Hills Muir of Dinnett, Ariundle, Tarbat Ness	mudstone (lamin.)	2583-3007 (excl.Sf)	-4085 -4118	205 (22)
8	Knockfarril Hill (KHm, 15x)	Foulden, Fountainhall (Mary Anning area)	sandstone	2824-2885	-4126 -4128	166 (19)
7	Jura (Jm)/GT (61x)	Aucherarder, Crail; Aberlady drill hole 2	mudstone	2333-2419	-4150 -4157	222 (7)
6	Jura (Jm)/VRRb (11x)	Quarry Haven	mudstone	2171-2279	-4144 -4150	209 (33)
	Pettegrove Point (PPm)/VRRa (6x)	Ben Arkle	mudstone	2129-2152	-4168 -4170	324 (107)
5?	Hartmann's Valley (HVm, 7x)	Eiseb, Palmhorst	sandstone	1275-1276	-4426.5 -4427.4	261 (36)
4	Pahrump Hills (basis) (PHm, 11x)	Hayden Peak, Ibex Pass 785	mudstone	740-800	-4454 -4461	291 (63)
3	Kimberley (Kf, 44x)	Neil, Stephen, Nullara, Harms, Liga; Nita, Angelo	sandstone & conglom.	544-626	-4478 -4488	416 (27)
2	'Lower Bradbury' (31x)	Pebble, Dragons Teeth, Heimdall, Kasegalik	sandstone	335-401	-4501 -4511	303 (28)
1	YB/Sheepbed (14x)	Laddie, Redstone, John Klein RP3	mudstone	147-294	-4520.3 -4520.9	220 (22)

Figure 2. Stratigraphic column for crater floor (Aeolis Palus) and Mt. Sharp (Aeolis Mons) as explored by the Curiosity rover (Fedo et al., 2022). The plot on the left side (Cu327 peak areas vs. elevation) highlights the observation of 10 regions of Cu enhancements. The thick red line in that plot is proportional to the sum of all Cu327 peak areas that are encompassed in a "moving" 7.5-m wide box. It illustrates the variation of Cu abundance throughout the mission and was used to identify Cu enhancements on the stratigraphic column (see Section 3). The table to the right provides some more information on these Cu-rich regions. The number of Cu points given in column #2 of that table refers to all Cu points (including bedrock, float rocks, and diagenetic features) within the given sol and elevation range (columns #5 and #6). In other words, the elevation ranges given in column #6 refer to Cu detections and may therefore slightly deviate from those read from the stratigraphic column for the respective formations/members. The sol ranges in column #5 refer to the corresponding Cu detections and are also marked in the orbital maps in Figure S1 in Supporting Information S1. Cu enhancement #6 on the Vera Rubin ridge (VRR) includes two areas, labeled by "VRRa" and "VRRb", that are found below and above Jm/GT, respectively. The given sol ranges (column #5) for these two areas are the dominant ones, but they are not complete because the rover explored given Cu-enriched areas several times during its complex traverse on VRR (see list of all Cu-bearing targets in Table S2 in Supporting Information S1).

chemical signature and in particular in the ChemCam MOC predictions. As pointed out by Dehouck et al. (2022) this procedure is not perfect, but should be a useful first step to discard contaminated bedrock points.

4. Results

4.1. Detection of Copper Along the Rover Traverse

Ten regions of enhanced Cu abundance have been observed between landing and Sol 3007 (see Section 3 for the definition of these regions). Figure 2 (left part) displays these Cu-rich regions by combining the results of this work (Cu327 peak areas vs. elevation) with a high-level version of the stratigraphic column (Fedo et al., 2022). Cu-rich areas #3, #7, and #8 (as defined and labeled in the left part of Figure 2) are focused on in this work. The associated data table (right part of Figure 2) provides some more detailed information on these Cu enhancements, such as the members/formations, lithologies, and elevation ranges that host these Cu enhancements, the timing of ChemCam analyses during the mission (sol ranges), prominent Cu-bearing targets and estimated abundances (ppm) on the spatial scale of a single LIBS measurement (~300 μm).

Early in the mission, on Sols 45 and 48, that is, ~200 m East of the landing site, ChemCam data revealed the first clear evidence for copper in the float rock Jake Matijevic (6 ChemCam points with an average abundance of ~270 ppm Cu) that had initially been interpreted as a fractionated alkaline igneous rock (Stolper et al., 2013). The rover continued ~200 m eastwards, descending into YB, which is among the lowest areas in the crater. This

area was found to be rich in clay minerals (Bristow et al., 2015; Vaniman et al., 2014) that had not been detected from the orbit. The area is interpreted to have hosted a lake, where clay minerals formed in situ from basaltic precursor sediments during the lake's putative lifetime of thousands (or 10s of 1,000s) of years (Grotzinger et al., 2014, 2015; McLennan et al., 2014). YB was found to be enriched in Cu (typically ∼220 ppm). This Cu enhancement is labeled #1, as it is lowest on the stratigraphic column (Figure 2). From YB onwards, the rover drove more or less continuously uphill, first gaining ∼60 m in elevation traversing Bradbury group, thereafter ∼320 m in elevation throughout Murray formation. Additional locations of Cu enhancements (labeled "2" through "10", Figure 2) were observed during this ascent. Notably, Cu enhancements #2 and 3, referred to as "lower Bradbury" and "Kimberley" (300–400 ppm), represent the highest Cu abundances measured by ChemCam throughout the mission. These Cu enhancements appear as broad peaks in Figure 2. In particular, Cu enhancement #2 includes data points that have been acquired over a mission time of 66 sols and are spaced by up to 1.6 km on the Martian surface, but they appear as one broad peak because the rover gained only little elevation (∼10 m) during that traverse. Also, the above-mentioned Cu points on "Jake Matijevic" (not mentioned in the data table associated with Figure 2) are mixed into Cu enhancement #2.

After the exploration of Kimberley, Cu was sporadically detected at PHm, Hartmann's Valley, and on the VRR that belongs partly to the Pettegrove Point (PPm) and partly to the Jura member (Jm/GT/VRR, Figure 2). In contrast to these sporadic Cu detections (Cu enhancements #4–6), many Cu detections were made in GT (Jm/GT, KHm, and Gm) and in the cap rock (Sf) on the Greenheugh Pediment (Cu enhancements #7–10, Figure 2). There is a general lack of Cu detections in most of the Murray formation from mid-PHm up to PPm (Figure 2).

4.2. Detection of Copper in the Kimberley Area

The Cu points located in the Kimberley area have been analyzed by Payré et al. (2019). Here, we address a single aspect of that data set that will be instructive when discussing Cu abundances in GT. The detailed local stratigraphy for the Kimberley area was worked out by Rice et al. (2017). The two lower-most m of that stratigraphic column contain four members, referred to as Point Coulomb, Liga, Square Top, and Dillinger, respectively (Figure 3). The plots in Figures 3a and 3b (MnO abundance vs. Cu327 area, Cu324 vs. Cu327 areas) display strong geochemical differences between Liga and Dillinger. Cu-enriched Liga points were obtained on poorly sorted sandstone and conglomerate in the Liga member. However, Cu-enriched Dillinger points were not obtained on the fine- to medium-grained Dillinger sandstone, but mostly on fracture fills in that member. While Liga has slightly higher Cu abundances compared to Dillinger, the latter has a clear correlation between Mn and Cu that is completely absent in the former (Figure 3a). As explained above (see Section 2), precipitated Mn oxides (especially MnO_2) are among the solids/minerals that most strongly and efficiently scavenge Cu^{2+} ions from solution, and, indeed, Figure 3a suggests that preferred adsorption of Cu ions on Mn oxides caused the observed correlation between both elements. This conclusion has already been reached by Payré et al. (2019), although here we used the second Cu line (λ = 327.4 nm, rather than 324.8 nm, see Section 3) and obtained an even better linear regression. It is remarkable that such a correlation has not been observed again higher up on the stratigraphic column (beyond Kimberley, see Figure S6 in Supporting Information S1). This indicates that Cu enrichment in the Dillinger member/Kimberley formation is unique. Accordingly, we do not invoke the adsorption of Cu ions on MnO_2 in GT.

4.3. Detection of Copper in the Glen Torridon Area

As already emphasized above, the next significant Cu enrichment after Kimberley and PHm was found in GT (Bennett et al., 2022). Three important Cu-rich areas and corresponding bedrock types (labeled by A, B, and C, respectively, and circled by white dotted ellipses) are noticed (Figure 4): (A) a small area within the clay-rich Jm trough (also referred to as "smooth-ridged CBU" or "smooth-ridged CBU", Fedo et al., 2022), (B) the upper Gm and Sf (including the SP area), and (C) the DS near the MA drill site. The very same traverse throughout GT is also shown as a plot of elevation versus sol number (see Figure S3 in Supporting Information S1). Cu abundances in GT are low, that is, about half of those measured in Kimberley (Figure 2) and close to the LOQ (Figure 2), but significant in the sense that many Cu-bearing ChemCam points were located close to each other, especially in the low-lying trough of GT (Jm mudstone, region A) or on a specific meter-sized outcrop (KHm sandstone, region C). A more detailed analysis of Cu detections in Gm is difficult, as these Cu detections correspond to low Cu abundances (within the footprint of ChemCam LIBS, Section 3) and are scattered over a large area (∼1 km

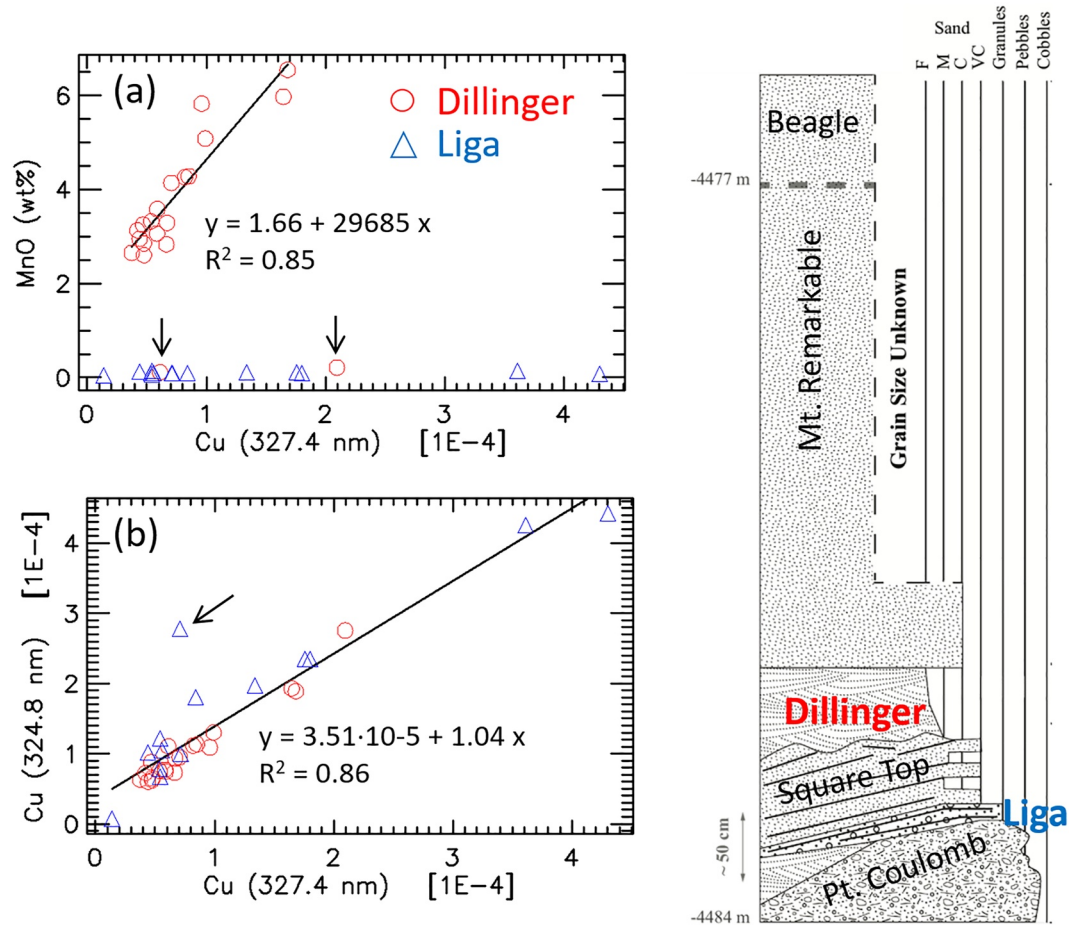

Figure 3. Geochemical properties of Dillinger (red circles) and Liga member (blue triangles) in the Kimberley formation next to the local stratigraphic column (Figure 5b in Rice et al., 2017 [slightly modified]). (a) MnO (wt%) versus Cu327 peak areas with a linear fit though the Dillinger points (as listed in Table 1 in Payré et al., 2019). Two outliers (Wallal and Blina, black arrows) have been ignored for the linear fit. (b) Cu324 versus Cu327 peak areas with a linear fit through all points—including the outlier marked by black arrow (discarding that outlier would result in $R^2 = 0.95$). The slope of that line is close to 1.0, which is the value expected from the NIST data base.

in size, Figure 4). A detailed analysis of Cu detections in Stimson sandstone (region B) is hindered by the small data set (the Stimson campaign was short, see Section 2) and is also beyond the main focus of this work, since the Greenheugh pediment (including its Stimson sandstone) is outside GT.

Table 1 shows the distribution of ChemCam Cu points among different geologic units. No Cu was found in dedicated "soil targets", that is, targets that were selected with the intent to analyze Martian soil. In all three GT stratigraphic members, most Cu points have been acquired on bedrock. This is not the case for the Sf, which may simply be due to low statistics which, in turn, may reflect the short duration of the Stimson campaign (Sol 2695–2732, i.e., less than 6 weeks). The column entitled "float rocks" (Table 1) would naturally also contain iron meteorites, but Cu was not detected in any of the iron meteorites observed along the traverse. According to Table 1, five Cu-bearing ChemCam points on float rocks were found in Gm, of which three also contain Ni and belong to the same target "Gretna Green ccam" (Sol 2608) that based on visual appearance and chemical composition might be a chondritic meteorite (Lasue et al., 2020). Figure 5 focuses on Ni-bearing ChemCam points, including those on "Gretna Green ccam". It shows that Fe meteorites contain Ni but no detectable Cu (as mentioned above). It also shows, although at low statistics, that Cu- and Ni-bearing ChemCam points have Fe abundances close to Mt. Sharp average. Gretna Green ccam is located in a field (labeled "a") in that diagram (Figure 5), where we may expect more chondritic meteorites.

The fifth column of Table 1 (diagenetic features) mentions two Cu-bearing Ca sulfate veins: Bighouse and Lealt (see Figure S4 in Supporting Information S1 for ChemCam spectra and images).

Figure 4. Map of Glen Torridon (GT) showing the relative distribution of Cu (by colored dots). Zoomed-out versions of this map can be found in Figure S1 in Supporting Information S1. The high part of the Vera Rubin ridge (VRR) and the lowest area of GT ("smooth-ridged CBU") correspond approximately to the Jura member (Fedo et al., 2022). Two Cu-enriched areas on VRR are also shown for completeness (Figure 2). The rover traverse through GT was divided into segments of 10 m, and in each of these intervals the Cu327 peak areas were summed up. Finally, the data were scaled to a maximum value of 10 and stretched within the interval "average ± standard deviation". The entire rover traverse in GT has a length of ~4,100 m. Thus, ~410 data points were computed, but most of them are equal to zero and are therefore not shown in this map. 3 Cu-rich areas are labeled by A, B, and C and highlighted by white dotted ellipses. The three white dotted arrows in area A represent, respectively, the left border, the center (marked by a lower-case "c".), and the right border of the image mosaic in Figure 6a. Area B is partly outside GT. Abbreviations: CBU = Clay-Bearing Unit, Jm = Jura member, KHm = Knockfarril Hill member, Gm = Glasgow member, Sf = Stimson formation; DS = Dark Strata. Credit: NASA/JPL. HiRISE Team, Univ. Arizona. https://mars.nasa.gov/maps/location/?mission=MSL.

The final part of this section will focus on bedrock (including Cu-bearing bedrock) in Jm/GT and KHm. Figure 6a conveys a qualitative impression of the relative importance (in area coverage) of coherent and rubbly bedrock in Jm/GT, while Figures 6b–6e shows their Harker diagrams for Mg, K, Fe, and Mn. Importantly, for the sake of this work, the Harker diagrams clearly demonstrate that Cu points (colored in Figure 6a according to Cu327 peak areas) only appear in coherent, not in rubbly bedrock. Since rubbly bedrock could not be drilled, we are missing detailed (X-ray-diffraction based) mineralogical information on that bedrock that would have

Table 1
Distribution of Cu-Bearing ChemCam Points Among Different Geologic Units in Glen Torridon

Formation/member	*N* (all)	*N* (bedrock)	*N* (float rocks)	*N* (diagenetic features)	*N* (other)
Stimson formation (Sf)	10	2	3	0	5
Glasgow member (Gm)	24	15	5	0	4
Knockfarril Hill member (KHm)	27	18	0	2	7
Jura member (Jm)	61	38	0	0	23
Sum	122	73	8	2	39

Note. The classification of these ChemCam points was based on the images and on the chemical composition (MOC data). Two points in the Knockfarril Hill member were located on diagenetic features (Bighouse/point 4 and Lealt/point 1, see their respective images and spectra in Figure S4 in Supporting Information S1). Some points (right-most column) could not be classified, because their images did not allow for a unique classification (e.g., due to insufficient spatial resolution or unfavorable lighting conditions), because their chemical composition was not enough diagnostic to guide the classification, or because these Cu-bearing points/targets were deemed to be nonrepresentative of the respective stratigraphic formation/member. Details on these points can be found in Table S3 in Supporting Information S1.

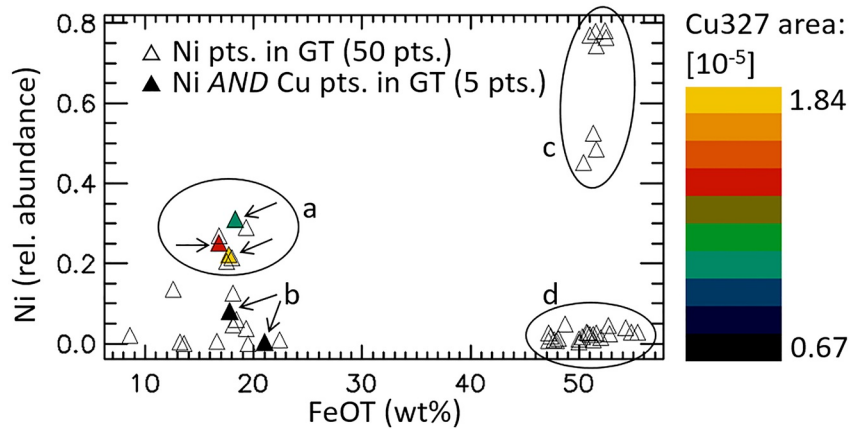

Figure 5. Cu- and Ni-bearing ChemCam points in GT (filled colored triangles, colored according to Cu327 peak area, see colorbar) plotted with Ni-bearing ChemCam points (empty triangles). The relative abundances of Ni (vertical axis) were computed as correlation scores with a pure Ni spectrum. The total iron oxide abundances (FeOT, horizontal axis) are the MOC (Major Oxide Composition) predictions and are likely underestimated for the high-Fe targets (FeOT >40 wt%) in this plot (David et al., 2020). a = float rock Gretna Green ccam, Gm (possibly a chondritic meteorite, all 7 points within area "a" belong to the same target, i.e., Gretna Green ccam, 3 of those 7 points contain both Ni and Cu). b = mixtures of soil/bedrock, KHm (Mary Anning 2 ccam, Black Mire). c = Fe meteorites. d = dark veins, Gm (Abernethy ccam, Roxburgshire, and Dunbartonshire, see Gasda et al., 2022).

been returned by the CheMin instrument onboard the rover. However, ChemCam returned a large amount of data on both types of bedrock and the Harker diagrams demonstrate that coherent bedrock is enriched in Mg, Mn, Cu, strongly depleted in K, and slightly depleted in Fe (as compared to rubbly bedrock; see also Dehouck et al., 2022). These results are largely confirmed by APXS data (Gellert, 2013; O'Connell-Cooper et al., 2020). In particular, the higher abundances of rubbly bedrock in Fe and its lower abundances in Mn imply a higher ratio Fe/Mn for rubbly bedrock (as compared to coherent bedrock). The ratio Fe/Mn has been used as a proxy for the chemical alteration of Martian bedrock (Brückner et al., 2005; Yen et al., 2010). Therefore, in the Jm/GT member and based on this proxy, rubbly bedrock is more altered than coherent bedrock. This result contrasts with the Chemical Indices of Alteration (CIA, Nesbitt & Young, 1982) that are rather similar for both types of bedrock (Table 2; see also Dehouck et al., 2022). The reason for this discrepancy is not well understood. However, we suggest that the Fe/Mn ratio records a different type of alteration than the CIA.

As explained earlier (see Section 2), coherent bedrock is a minor bedrock facies in Jm/GT, but becomes the dominant one in KHm. Given the strong Cu signature in coherent Jm/GT bedrock, we expected an equally strong Cu signal in coherent KHm bedrock, but this was not observed: the Cu detections at stratigraphic levels beyond Jm/GT (including Cu detections in coherent KHm bedrock) were significantly weaker than in Jm/GT and their distribution turned out to be more complex.

Figure 7 describes Cu detections in KHm. Figure 7a shows the Cu-enriched "Outcrop B" (including the "DS") which is located about 2 m west of the actual MA outcrop, named "Outcrop A" (Figure S5 in Supporting Information S1), while Figures 7b–7e plots Cu detections (red double circles for the DS and black double circles, referred to as "ordinary Cu points", for all the other targets) on top of three different types of bedrock that were encountered in KHm: rubbly bedrock (br, green plus signs), coherent bedrock GE (bc-GE, red squares), and coherent bedrock MA (bc-MA, ochre squares). The point cloud representing rubbly bedrock contains data acquired along more than a kilometer of rover traverse in KHm (in the sol range 2474–2940), while the other two point clouds represent data from, respectively, 2 m-sized outcrops and their near vicinity (GE and MA). These data clouds serve as a reference frame that allows us to put the Cu data into context. Figures 7b–7e demonstrates the following geochemical trends: bc-MA < bc-GE < br (for Si), bc-MA < bc-GE < br (for Fe and K), and bc-MA > bc-GE > br (for Mg and Mn). These inequalities imply the following trend for the ratio Fe/Mn: bc-MA < bc-GE < br. Thus, also in the KHm member, rubbly bedrock appears to be more altered than coherent bedrock. Again, as in the above-discussed case of Jm/GT, this statement is not supported by the CIA values, which are similar for both types of bedrock (Table 2; Dehouck et al., 2022).

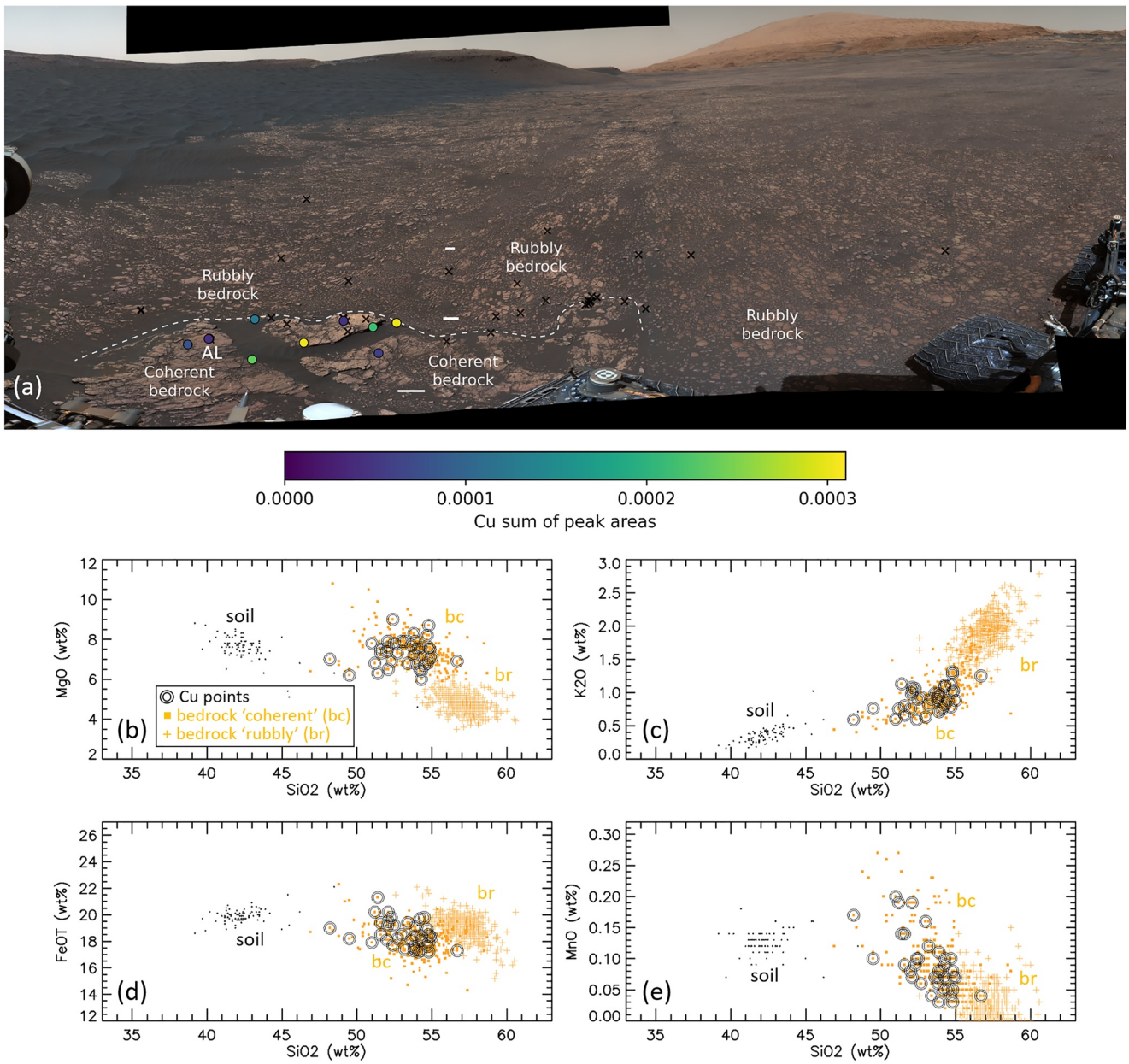

Figure 6. Coherent and rubbly bedrock in Jm (smooth-ridged CBU). (a) Panorama image (Sol 2375, ML, mcam12601) that displays Cu-bearing ChemCam points (colored according to the sum of Cu327 peak areas in a given target, AL = Aberlady, one of the two drill holes in coherent bedrock, Bennett et al., 2022; Dehouck et al., 2022) as well as ChemCam points where no Cu was detected (black crosses). This panorama image spans about 230°. Its two borders and its center are marked by, respectively, three white dotted arrows in Figure 4. The three white scalebars in the lower part of the image represent 100 mm. Credit: NASA/Caltech-JPL/MSSS. Compare the panel (a) to a similar compositional map (wt% MgO) in Dehouck et al. (2022). Panels (b–e) are the Harker plots (SiO_2 abundances on the horizontal axis) for MgO, K_2O, FeOT, and MnO with Cu-bearing points plotted on top of data for coherent and rubbly bedrock (as defined in Section 3). These panels demonstrate that coherent bedrock is enriched in Cu.

Comparing Figures 7b–7e to the analogous figure for Jm/GT (Figures 6b–6e) we can see that KHm bedrock is more diverse than Jm/GT bedrock, that is, its ChemCam points cover a larger area in the Harker plots, even though their averages are similar to those obtained in Jm/GT. Twelve "ordinary Cu points" (black double circles in Figures 7b–7e) plot mainly on top of bc-MA (rather than bc-GE or br) with 5 and 7 Cu points being located, respectively, on Outcrop B and in some other place in KHm (not Outcrop B). These "ordinary Cu points" have been acquired over more than a kilometer of rover traverse (Sol 2440–2942) and contrast with 38 Cu points in Jm/GT that are clustered in a few places within only 150 m of rover traverse (Figure 4). None of these "ordinary

Table 2
Chemical Composition of Different Types of Bedrock in Various Formations and Members With Focus on Cu-Bearing Bedrock as Well as Coherent and Rubbly Bedrock in General

Formation, member	Subset (bedrock)	*N*	SiO_2 (wt%)	TiO (wt%)	Al_2O_3 (wt%)	FeOT (wt%)	MgO (wt%)	CaO (wt%)	Na_2O (wt%)	K_2O (wt%)	MnO (wt%)	Sum (%)	CIA	Cu (ppm)
Sf	**Cu-bearing**	**2**	**49.80 (0.70)**	**0.74 (0.02)**	**10.75 (2.15)**	**18.00 (1.50)**	**10.05 (2.65)**	**3.20 (0.80)**	**2.94 (0.45)**	**0.75 (0.32)**	**0.30 (0.15)**	**96.53 (1.82)**	**47.92 (5.83)**	**188 (132)**
	All	233	43.74 (0.24)	0.93 (0.02)	9.43 (0.18)	20.91 (0.24)	8.67 (0.19)	4.01 (0.08)	2.89 (0.05)	0.59 (0.02)	0.32 (0.04)	91.50 (0.24)	42.32 (0.34)	–
Gm	**Cu-bearing**	**15**	**50.16 (1.41)**	**0.95 (0.02)**	**10.30 (0.47)**	**20.57 (1.16)**	**4.13 (0.48)**	**1.78 (0.19)**	**2.54 (0.10)**	**1.24 (0.10)**	**0.05 (0.01)**	**91.74 (1.53)**	**54.25 (0.74)**	**226 (28)**
	All	1,387	53.96 (0.10)	0.98 (0.003)	12.07 (0.04)	18.48 (0.07)	4.96 (0.03)	2.52 (0.04)	2.82 (0.01)	1.34 (0.01)	0.07 (0.006)	97.19 (0.10)	53.46 (0.13)	–
KHm	**Cu-bearing**	**18**	50.77 (1.10)	**0.94 (0.07)**	**10.04 (0.40)**	18.93 (0.56)	7.30 (0.35)	**1.58 (0.10)**	**2.36 (0.08)**	0.95 (0.09)	0.10 (0.02)	92.99 (1.35)	**56.33 (0.57)**	**183 (20)**
	Coherent/all	776	53.57 (0.11)	0.94 (0.005)	10.96 (0.04)	18.04 (0.06)	8.06 (0.06)	1.72 (0.03)	2.38 (0.01)	1.28 (0.02)	0.26 (0.02)	97.20 (0.12)	56.65 (0.10)	–
	Rubbly/all	129	56.63 (0.10)	0.99 (0.007)	11.50 (0.10)	18.91 (0.11)	5.15 (0.09)	1.23 (0.04)	2.63 (0.02)	1.89 (0.03)	0.02 (0.003)	98.95 (0.20)	57.21 (0.17)	-
	All	905	54.01 (0.10)	0.95 (0.004)	11.03 (0.04)	18.16 (0.06)	7.65 (0.07)	1.65 (0.02)	2.41 (0.01)	1.37 (0.02)	0.22 (0.02)	97.45 (0.11)	56.73 (0.09)	–
Jm	**Cu-bearing**	**38**	53.19 (0.27)	**0.94 (0.02)**	**11.64 (0.16)**	18.53 (0.16)	7.31 (0.11)	**2.09 (0.15)**	**2.58 (0.03)**	0.91 (0.03)	0.13 (0.04)	97.35 (0.31)	**56.51 (0.64)**	**225 (9)**
	Coherent/all	297	53.83 (0.10)	1.02 (0.02)	11.84 (0.07)	18.11 (0.06)	7.42 (0.04)	2.02 (0.04)	2.65 (0.02)	0.99 (0.02)	0.10 (0.007)	97.97 (0.12)	56.62 (0.19)	–
	Rubbly/all	367	57.12 (0.06)	0.97 (0.004)	11.92 (0.05)	19.13 (0.05)	4.82 (0.03)	1.21 (0.02)	2.64 (0.01)	1.91 (0.01)	0.03 (0.001)	99.76 (0.09)	58.01 (0.10)	–
	All	848	55.67 (0.07)	0.99 (0.007)	11.80 (0.04)	18.70 (0.04)	6.03 (0.05)	1.55 (0.02)	2.61 (0.01)	1.50 (0.02)	0.05 (0.003)	98.90 (0.07)	57.49 (0.09)	–

Note. Also provided are the Chemical Index of Alteration (CIA) as well as Cu abundances (in ppm) as inferred from peak fitting and univariate calibration (Payré et al., 2019, see also the Section 3). Numbers in parentheses are standard errors of the mean value. The table is sorted according to stratigraphic height (Jura on the bottom, Stimson on top). The label "all" indicates that Cu-bearing and nonCu-bearing bedrock has been taken into account. Rows in bold face refer to Cu-bearing bedrock. Data in red are discussed in the text and are also covered by Figures 6b–6e and 7b–7e. In particular, we chose "coherent bedrock in KHm" (776 ChemCam points) to be the bedrock at Glen Etive and at Mary Anning, which are the two KHm drill areas. Cu detections in the buttes area in KHm have been discarded in this table, since this area has a different chemical composition (Dehouck et al., 2022).

Cu points" were located on Outcrop A including its southeastern part (Ayton/Groken) that was found to be rich in Mn and P (see Section 2; Gasda et al., 2022). Given the dense ChemCam coverage of Outcrop A (several hundreds of ChemCam points) we can safely assume that Outcrop A is not enriched and may even be depleted in Cu.

Besides these "ordinary Cu points", Figures 7b–7e shows the DS Cu points that are marked by double red circles and additionally highlighted by a red contour. These Cu points include 4 points on Foulden (Fd, one of those points being located on a vein and marked by a dashed line in Figure 7d), 2 points on Woodside (W) and 1 point on Formartine (Ft) and have a distinct geochemical signature: they are particularly low in Si, Mg, and K, high in Fe and fairly low in Mn, that is, they have Mn abundances near the lower end of those of bc-MA (Figure 7e). Not surprisingly, their low SiO_2 concentration correlates with lower totals that are typically in the 80%–90% range. We emphasize that these double red circles are not just "statistical outliers", but reflect the specific geochemistry of a small local area (less than a meter across, see Figure S5 in Supporting Information S1) that has a significantly different visual appearance (as compared to surrounding bedrock). Note specifically the dark eroded rim of the target "W" (inset in Figure 7a). We also highlight target Prestonpans (P), a compact, high-silica, and relatively bright target compared to surrounding bedrock labeled by the letter "P" and marked by an arrow in Figures 7b–7e. This target does not necessarily represent "typical coherent bedrock", but it is located close to the "DS" (Figure 7a) and highlights even more the diversity of Outcrop B (Figure S5 in Supporting Information S1).

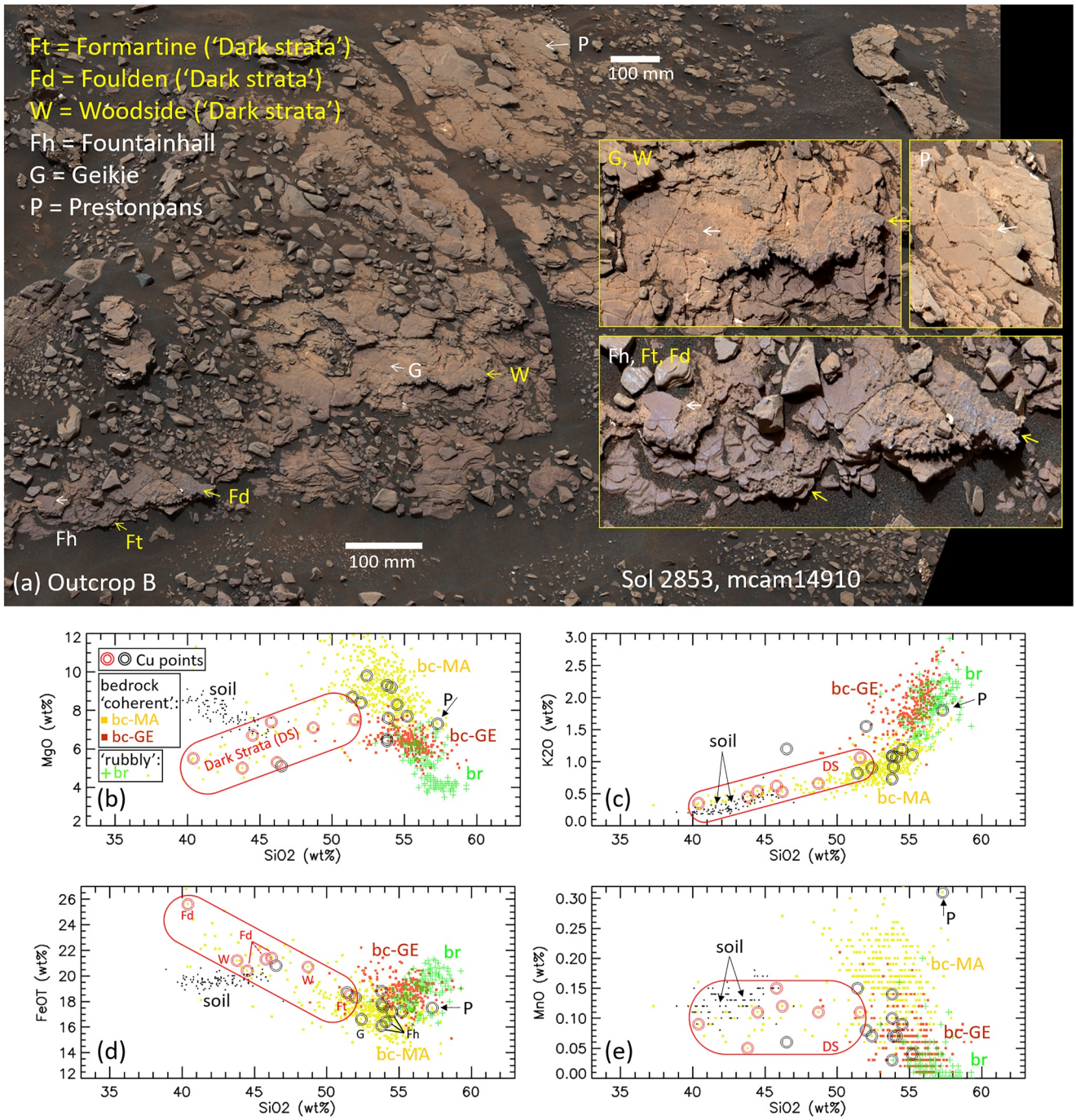

Figure 7. Coherent and rubbly bedrock in KHm. (a) Background image showing all targets on "Outcrop B" that is located right next to "Outcrop A", the Mary Anning (MA) drill outcrop (see map in Figure S5 in Supporting Information S1). In the background image, each arrow marks point #1 of the ChemCam raster and has a length that approximately matches the length of the linear ChemCam raster. In the insets (G and W; P; Fh, Ft, and Fd), the arrows are located slightly off the target in order not to cover any features of the bedrock. Background image: Sol 2853, ML, mcam14910, insets: Sol 2853, MR, mcam14910 (the vantage point is slightly different for the insets as compared to the background image). Credit: NASA/Caltech-JPL/MSSS. Panels (b–e) are the Harker plots (SiO_2 abundances on the horizontal axis) for MgO, K_2O, FeOT, and MnO. As in Figure 6 Cu-bearing points are plotted on top of bedrock data. Panels (b–e) demonstrate the larger diversity of KHm bedrock as compared to Jura bedrock (Figure 6). Overall, Cu-bearing points plot on top of Mary Anning (MA) bedrock, not Glen Etive (GE) bedrock. Cu-bearing points in the Dark Strata (red double circles) are highlighted by a red contour and differ geochemically from the other Cu-bearing points (black double circles). Panel (d) is used to label some important targets on Outcrop B (these labels are explained in panel (a)). Further abbreviations: bc-MA = bedrock "coherent" Mary Anning, bc-GE = bedrock "coherent" Glen Etive, br = bedrock "rubbly". The data labeled "bc-MA" excludes the ChemCam target "Ayton" (located on the Mary Anning outcrop near the Groken drill hole) and Ayton-like bedrock (Dehouck et al., 2022).

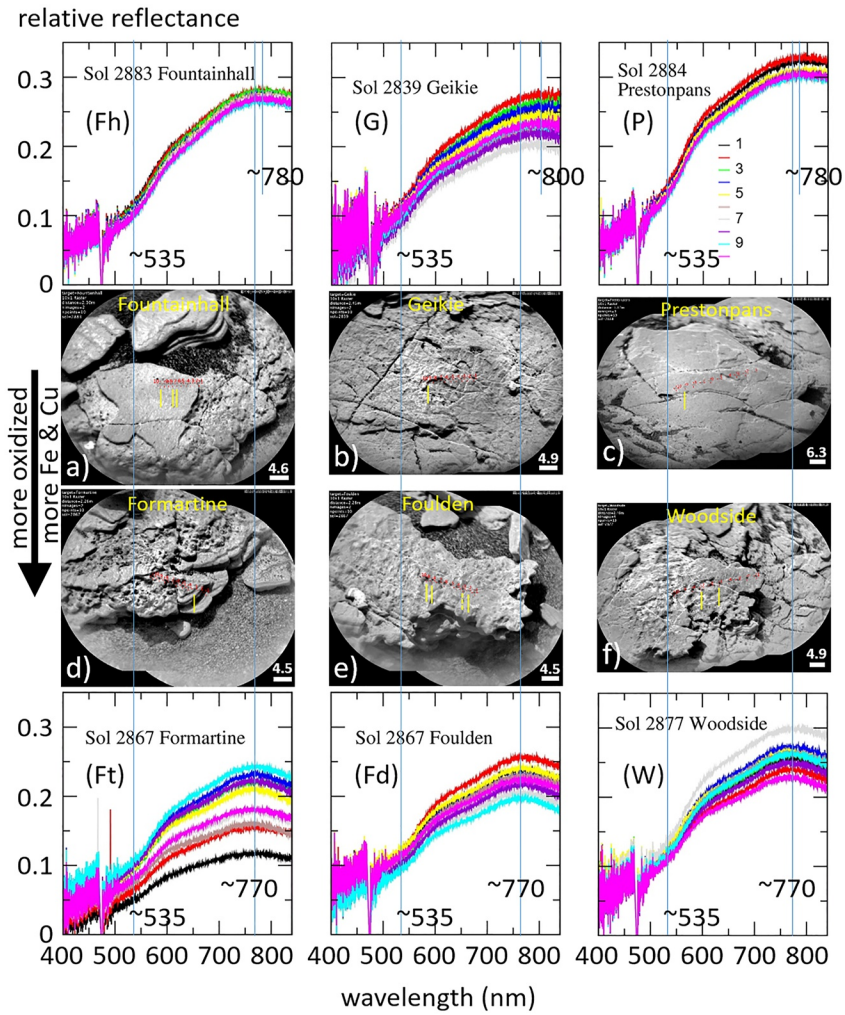

Figure 8. Surface texture, reflectance spectra, and inferred oxidation state of the most important targets on Outcrop B (Dark Strata area). The yellow lines in the images point to Cu-bearing ChemCam points. The lengths of the scalebars are given in millimeter. Based on visual appearance and reflectance spectra, these targets fall into two groups: (a–c) relatively bright, compact, smooth-platy, less oxidized and (d and e) dark, eroded, nodular, more oxidized. The latter group of targets is more abundant in iron and copper (Figure 7d).

Figure 8 shows high-resolution (RMI) images and ChemCam passive spectra (Section 3) of targets on Outcrop B (including the DS). Based on their reflectance spectra, we distinguish between two classes of targets:

1. targets that we refer to as "coherent/Outcrop B" (Fountainhall (Fh), Geikie (G), P, Figures 8a–8c): their reflectance spectra display a very weak 535-nm band and a weak maximum at wavelengths longer than 770 nm, and
2. the DS targets (Ft, Fd, and W, Figures 8d–8f): their reflectance spectra have a significant band depth at 535 nm and a more pronounced maximum at 770 nm.

The spectral properties of these two classes of targets correlate with their visual appearance, since the former are compact and smooth-platy, while the actual DS targets represent the dark, eroded edge of the outcrop and have a nodular texture. Importantly, the spectral properties (Figure 8) suggest that the DS targets are more oxidized than "coherent/Outcrop B", that is, they not only contain considerably more Fe (in average ~21 wt% FeOT as opposed to ~17 wt% in "coherent/Outcrop B") but also contain a crystalline ferric-oxide phase. In addition, the DS targets were significantly more enriched in Cu (>200 ppm) than "coherent/Outcrop B".

Figure 7e suggests that Cu in the DS targets is *not* correlated with Mn, as is the case in the Dillinger member/Kimberley (see also Figures S6c and S6h in Supporting Information S1). This is somehow surprising since dissolved Cu (Cu^{2+}) is known to have a strong affinity to Mn oxides (Section 2). We conclude that the DS targets

record a different type of Cu enrichment than the earlier discussed targets in the Dillinger member. We also note that the nearby Groken drill area in Outcrop A is enriched in Mn and P (Gasda et al., 2022). Hence, ChemCam data led to the discovery of two patches of outcrop that are within ~2 m from each other (Figure S5 in Supporting Information S1) and appear to have a very different chemical signature: Cu/Fe-rich targets (DS) on the one hand and Mn/P-rich targets (Ayton/Groken) on the other hand (Gasda et al., 2022).

Some of the above-mentioned differences between Jm/GT and KHm can also be seen in Table 2. Starting from the lowest member (Jm/GT), we can see that Cu-bearing bedrock is very consistent with coherent bedrock in general in terms of major-oxide abundances, totals and CIA. Transitioning to KHm, this consistency is partly lost because (a) the DS (7 Cu points) have an unusual composition (as discussed above), and (b) "coherent rock" in KHm is not as homogeneous as in Jm (e.g., see different composition of Glen Etive (bc-GE) and Mary Anning (bc-MA), Figures 7b–7e). In particular, the Cu-bearing bedrock in KHm has lower silica and lower totals than coherent KHm bedrock in general, which is influenced by the DS points in this group. Note that the CIA of Cu-bearing KHm bedrock does not seem to be affected by the low totals.

Table 2 reports 15 Cu points spread over a larger area in the Gm and two Cu points in the Stimson sandstone (Sf). The latter two Cu points have a significantly higher SiO_2 concentration than the average of all (233) Sf bedrock points. We cannot explain this observation. However, due to low statistics (only 2 Cu points on Sf bedrock), it remains unclear if this is a coincidence or if it applies to Cu-bearing Sf bedrock in general. Significant differences between Sf bedrock and GT sediments are expected, since the former has a completely different lithology and may also have different provenance (Banham et al., 2018, 2021, 2022; Bedford, Schwenzer, et al., 2019; Bedford et al., 2020, 2022; Bennett et al., 2022).

Finally, we compare the number of ChemCam Cu points to the total number of ChemCam points on specific types of bedrock. According to Table 3, the fraction of Cu detections in Jm/GT reached 4.5%, but when only considering bedrock, the fraction dropped to 1.3%. The same applies to Cu detections in Sf: 2.3% Cu detections for all types of surface units, but only 0.9% for bedrock targets. This implies that a considerable part of Cu detections in Jm/GT and Sf has been on detritus, diagenetic features (e.g., Ca sulfate veins, Figure S4 in Supporting Information S1) and poorly defined mixtures of soil and bedrock rather than true bedrock (as defined in the Section 3). The high fraction of Cu points (2.2%) in MA bedrock is mainly due to the Cu points on Outcrop B.

5. Discussion

The most significant results of this work are the following:

1. The Cu enrichments observed in Jm/GT and KHm are low: typically ~200 ppm (Figure 2, Table 2). However, they are significant from a statistical as well as geochemical point of view, as this value is likely (at least) 10 times higher than the Cu background level. This statement is supported by the fact that most SNC meteorites have even lower Cu abundances (see Section 2). ChemCam cannot directly measure that background level (the Limits of Detection and Quantification are, respectively, LOD ~ 50 ppm, LOQ ~ 200 ppm, see Section 3). Further down in the Liga member/Kimberley formation, Cu levels approach 400 ppm (Figure 2), still very low abundance with respect to commercial Cu deposits on Earth.
2. Starting in Jm, the lowermost stratigraphic member in GT, we observed Cu enrichment only in coherent bedrock, whereas no Cu was detected in rubbly bedrock.
3. Higher up in the next stratigraphic member (KHm), coherent bedrock showed up in (at least) two different flavors, that is, GE and MA. It turned out that Cu was mainly enriched in MA-like bedrock (Figures 7b–7e) but not in the actual MA outcrop (called "Outcrop A", Figure S5 in Supporting Information S1). We also noted that Cu detections in KHm were less frequent, occurred over a larger area and had lower abundances (in ppm) than those in Jm/GT.
4. Specifically in the MA area (KHm), we found two areas located about two m from each other that have very different geochemical properties: "Ayton/Groken on Outcrop A", enriched in Mn and P (with no detection of Cu), and the "DS/Outcrop B", enriched in Fe and Cu.

In this section, we attempt to place these observations in a broader context that potentially will also shed light on the formation and alteration history of coherent and rubbly bedrock in both Jm/GT and KHm.

Figure 9 shows the Pourbaix diagram for the system Cu-Fe-Mn-H_2O. It can be seen that the stability field for dissolved Cu^{2+} is roughly defined by a bent subhorizontal line (extending from pH = 0 through ~7) and a vertical

Table 3
Number of All ChemCam Points and Cu-Bearing ChemCam Points in Various Stratigraphic Formations and Members With Special Focus on Bedrock and Different Types of Bedrock

Formation/member	Subset	*N* (all points)	*N* (Cu points)	Fraction (%) of Cu points
Sf	All bedrock	233	2	0.9
	All	**432**	**10**	2.3
Gm	Bedrock	1,387	15	1.1
	All	**2,351**	**24**	**1.0**
KHm-Gm transition	Bedrock	86	0	0
	All	**115**	**0**	**0**
KHm	Bedrock (Teal Ridge)	59	1	1.7 (low statistics)
	Bedrock (Harlaw Rise)	118	4	3.4 (low statistics)
	Bedrock (Glen Etive)	274	0	0
	Bedrock (Mary Anning)	502	11	2.2
	Bedrock (Rubbly)	129	0	0
	All	**2,638**	**27**	**1.0**
Jm	Coherent bedrock	297	38	1.3
	Rubbly bedrock	367	0	0
	Flodigarry facies bedrock	184	0	0
	All	**1,362**	**61**	4.5
Sum	**All**	**6,898**	**122**	**1.8**

Note. The label "all" indicates that all types of surface material (float rocks, bedrock, diagenetic features, etc.) have been taken into account. The main goal of this table is to document the fraction of ChemCam points that revealed presence of Cu (right-most column). These fractions may be considered as a proxy for Cu abundance and may be compared to concentrations (ppm Cu) in Table 2. Again, like in Table 2, only good-quality ChemCam data have been used to compile this data table and an effort has been made to ensure consistency with similar data tables in Dehouck et al. (2022). Some of the numbers in this table can also be found in Table 2. KHm bedrock is of coherent type, unless stated otherwise. Data on all surface units (including bedrock, float rocks, and diagenetic features) are highlighted in bold face. The fractions of Cu points are highlighted in red, when they are higher than the fraction for all ChemCam points (1.8%).

straight line at pH ∼ 7. The subhorizontal line does not vary much, neither as a function of temperature (at least within the interval 0°C–25°C) nor as a function of Cu^{2+} concentration. However, the vertical line moves slightly to the left by ∼0.4 pH units when increasing the temperature from 5°C to 25°C (as shown in Figure 9). The effect of Cu^{2+} concentration is more significant: When increasing the concentration by a factor of 100, the vertical line moves typically by 1 pH unit to the left (and vice-versa). We chose to display the case of a concentration of 10^{-6} mol/L for two reasons: (a) this is a standard value for ionic concentrations used in Pourbaix diagrams in the literature and, more importantly, (b) we assume that Cu-bearing fluids in the GT area were probably much poorer in Cu than we would expect in "Cu-enriched" geological settings on Earth (see Section 2). For reference, ore-forming hydrothermal solutions on Earth typically contain 10^{-3} to 10^{-2} mol/L Cu^{2+} (Pohl, 2011, p. 186). Given the low Cu abundances in the GT area (∼200 ppm, see above), we hypothesize a much smaller concentration for the fluids that transported and redistributed Cu, for example, 10^{-6} mol/L (as in Figure 9), or even down to 10^{-8} mol/L Cu^{2+}.

Caravaca et al. (2022) and Fedo et al. (2022) provided evidence that Jm/GT rubbly bedrock was deposited in shallow water and in a low-energy, mostly lacustrine environment. Over the next 10–20 m in elevation and further south the bedrock facies gradually changed from vein-free mudstone to a variety of different types of sandstones, reflecting the transition to a higher-energy depositional environment. These sandstones, referred to as the KHm, generally exhibited a network of veins and appeared to be more cemented and more resistant against erosion. Caravaca et al. (2022) hypothesized that this significant change in bedrock facies may be caused by a drop in lake level and may even reflect a global change in Martian climate. Their model allows for significant differences between Jm-type mudstone and KHm-type sandstone as well as within the KHm-type sandstones themselves. In particular, the dynamism of the depositional environment may have had direct consequences on the chemical

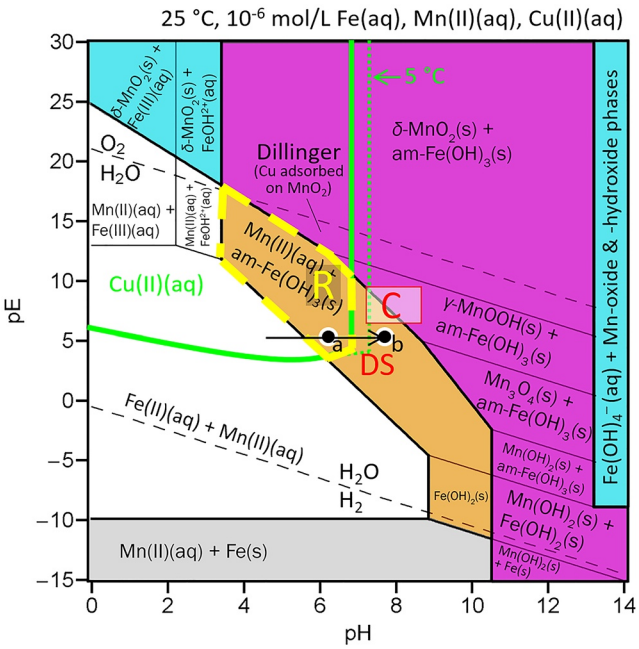

Figure 9. Pourbaix diagram (pE vs. pH, E[V] ≈ 0.059·pE) for the Cu-Fe-Mn-H_2O system at standard conditions and for 10^{-6} mol/L aqueous solutions. The top left domain delimited by the thick solid green line is the stability field for dissolved Cu^{2+} (Beverskog & Puigdomenech, 1995, 1997; Payré et al., 2019). Outside that domain, depending on ionic species present, a variety of Cu-bearing solid phases (including native Cu and various Cu oxides) would be stable. This diagram attempts to explain some characteristics of selected rock types in the Kimberley and Glen Torridon areas assuming in situ open-system alteration rather than provenance effects or sorting effects during transport. Based on this assumption, the Cu signature of Dillinger sandstone (upper part of the diagram) would be caused by precipitation of Mn oxides from acidic fluids, while rubbly bedrock (R) and coherent bedrock (C) would have been affected by acidic and alkaline fluids, respectively. The black arrow (labeled "DS") marks two possibilities (a and/or b) for the postulated evolution of fluid chemistry that controlled the chemical signature of the Dark Strata bedrock (see main text). The position of that arrow on the vertical axis is not well constrained and could also be at higher pE values than shown in this figure.

and mineralogical composition of the bedrock, for example, by gravitational segregation of the bed load during transport or by chemical changes postdeposition as a result of different porosity and permeability. Furthermore, Jm/GT mudstone would be expected to be rather homogenous due to efficient mixing of suspended bed load prior to deposition, while different types of KHm sandstones might have inherited more strongly the chemical characteristics of their respective source regions. This is consistent with the observed higher diversity of KHm sandstones as compared to Jm/GT mudstone and is demonstrated by the geochemical differences between GE and MA sandstones in the KHm area (Dehouck et al., 2022).

In the following section, we assume that Cu was brought along from a Cu-rich source region, somewhere from the Northern crater rim or beyond that rim (Figure S1a in Supporting Information S1). This scenario was invoked by Payré et al. (2019) and may be the easiest hypothesis to explain Cu enrichment in Gale crater, both in the Kimberley and GT areas.

In this scenario, we can place the different Cu-enriched bedrock units in the pE-pH diagram (Figure 9). It was shown that Cu-enriched ChemCam points on fracture fill in the Dillinger member/Kimberley in Aeolis Palus (Section 4.2) showed a strong correlation between Cu and Mn (Figure 3a). We suggest that Mn^{2+}-bearing fluids encountered a strong oxidation potential in the area of the Dillinger member and precipitated Mn oxides. Cu^{2+} was removed from the solution by adsorption to these oxides (see area labeled "Dillinger" in Figure 9 that we favor for this process). In contrast, the even more strongly Cu-enriched points that were obtained on Liga sandstone and conglomerate (stratigraphically below the Dillinger member) did not show a correlation between Cu and Mn. The Dillinger member is characterized by low-angle cross stratification dipping to the north, which contrasts with the regional cross stratification dipping to the south. Therefore, Treiman et al. (2016) hypothesized that the Dillinger member may be of eolian origin and may have a different source region than most other sediments (including Liga) in this area. As a result, it seems likely that the enhanced Cu and Mn abundances in the Dillinger member would have been caused by the local redistribution of these elements, which would be consistent with their detection in fracture fills rather than bulk rock.

The "Dillinger" area (Figure 9) is bound at its high-pH side by the subvertical limit of Cu^{2+} solubility. We cannot exclude that Cu precipitation did actually happen beyond that limit, that is, at pH > 7. That scenario would imply slightly milder oxidative conditions. Mn enrichment in the fracture fills of the Dillinger member was also discussed by Lanza et al. (2016). Indeed, these authors favored a strongly oxidizing but slightly alkaline environment for the precipitation of Mn oxides (presumably MnO_2). In the former scenario (i.e., adsorption of dissolved Cu^{2+} on precipitated Mn oxides) we assume that Cu^{2+} adsorbed on these oxides would not be redissolved again, which might be a reasonable assumption since Mn oxides are known to have very strong affinity to Cu (~100% at pH ~ 6), with their affinity being even stronger than that of organic matter (see Section 2 in the present work, as well as Figure 15 in Bradl (2004)). However, the latter scenario would imply the coprecipitation of a Cu-bearing mineral (possibly an oxide) and a Mn oxide. In any case, both scenarios would be consistent with a strong correlation between Cu and Mn in the Dillinger member.

At higher stratigraphic levels a clear correlation between Cu and Mn has not been observed (Figure S6 in Supporting Information S1). Average MnO abundances are 0.20 ± 0.01 and 0.167 ± 0.004 wt% along the rover traverse through GT and along the entire rover traverse (up to Sol 3007), respectively, where the given uncertainties represent the standard error of the mean. Although Mn abundances are not a proxy for Cu abundances in the GT area, these MnO abundances are useful reference values when assessing the possibility of local depletion or enrichment in Mn.

The mineralogical analysis of the bedrock in both the Jm and KHm members indicates that the different types of bedrock in these members were formed at near-neutral to alkaline pH and in a somewhat more oxidizing environment compared to YB (Bristow et al., 2017, 2018; Thorpe et al., 2022). The ChemCam Cu detections demonstrate that these rocks were affected by mildly acidic to mildly alkaline fluids at a later stage during diagenesis and the locations of the labels "R" and "C" (denoting rubbly and coherent bedrock, respectively) in Figure 9 specify the suggested pE-pH properties of the respective fluids. In particular, based on the absence of Cu detections on rubbly bedrock, its low MnO abundances, and its slight enrichment in Fe as compared to coherent bedrock (Table 2, Figures 6 and 7) we suggest that rubbly bedrock was affected by slightly acidic oxidizing fluids in the orange zone of the diagram (pH ∼ 6).

In contrast to rubbly bedrock, there is no direct evidence that coherent bedrock was strongly depleted in Mn over the course of its diagenetic evolution (Table 2, Figures 6e and 7e). Taking into account the above given reference abundances for MnO, coherent bedrock may have been slightly depleted in Mn, but this could also be due to low Mn abundances in the source region. In the following, we will test the hypothesis that coherent bedrock mainly interacted with alkaline fluids (pH ∼ 8 or larger) such that Cu and Mn would have been immobile according to the pE-pH diagram in Figure 9. This would be consistent with the presence of small amounts of siderite in both Jura and Knockfarril Hill coherent bedrock (KM, GE 1, MA, MA 3, and Groken, Thorpe et al., 2022). In contrast to the alkaline fluids proposed for coherent bedrock, rubbly bedrock would have experienced a large-scale and substantial alteration/leaching by slightly acidic aqueous fluids. This interpretation would be consistent with our earlier observation that rubbly bedrock is more altered than coherent, where we used the ratio Fe/Mn as a proxy for chemical alteration of bedrock (see previous section).

Thorpe et al. (2022) developed a lacustrine-groundwater mixing model that explains the mineralogical composition of different stratigraphic members of GT in terms of subsurface mixing of slightly acidic lake water with alkaline ground water. Their work is largely based on x-ray diffraction data as returned by the CheMin instrument. Since no such data are available for rubbly bedrock, their model was developed based on coherent-bedrock data only (AB, KM, MA, MA 3, and Groken, see Section 2). In the following section, we will use some geochemical trends predicted by that model and assess how these trends can be linked to our observations of copper in GT.

A key parameter in Thorpe et al.'s (2022) model is the distance of the respective bedrock from the lacustrine-groundwater mixing zone. Their model predicts that bedrock closest to that mixing zone would have been altered by slightly acidic (pH ∼ 6.7) Fe- and SiO_2-rich lake water. In contrast, as the distance to the mixing zone increases, bedrock would be increasingly altered by high-pH, Mg-rich, Fe- and SiO_2-poor groundwater.

It is instructive to consider different bedrock facies in KHm, in particular rubbly bedrock and coherent GE- and MA-like bedrock, labeled as br, bc-GE, and bc-MA, respectively (as in Figures 7b–7e). Based on this work and that of Caravaca et al. (2022), it is reasonable to assume that rubbly bedrock would be closest to the lacustrine-groundwater mixing zone and the distance of each bedrock type to that mixing zone would increase in that order: br < bc-GE < bc-MA. Based on the lacustrine-groundwater mixing model, we would therefore expect the following geochemical trends: br < bc-GE < bc-MA (for Mg and pH) and br > bc-GE > bc-MA (for Fe and Si). In addition, we would expect rubbly bedrock to be most oxidized, as it would have been affected by oxidizing lake water. Indeed, all these assertions are fully consistent with the inferences that have been made here (see MOCs as plotted in Figures 7b–7e and the ratio Fe/Mn used as a proxy for chemical alteration) and that are partly illustrated by the pE-pH diagram in Figure 9. So far, this reasoning is based on KHm bedrock. However, the chemical composition of rubbly bedrock is very similar in either stratigraphic member (Jm/GT or KHm, see Table 2 and Figures 6b–6e and 7b–7e; see also Dehouck et al., 2022). Therefore, these geochemical trends apply to rubbly bedrock (br) in either member and despite the lack of CheMin data, rubbly bedrock can be reasonably described in the frame of this lacustrine-groundwater mixing model.

To this point, we have not yet addressed the role of coherent bedrock in Jm/GT in this model. As explained earlier, the "coherent-bedrock facies" already appears in Jm/GT, where it interfingers as a minor facies with the dominant "rubbly facies" (Caravaca et al., 2022), and it is the former facies where the Cu signal was found in GT. This observation led us to conclude that coherent bedrock in Jm/GT has mainly been affected by alkaline fluids (Figure 9). Another remarkable observation was the strict difference between coherent and rubbly bedrock in Jm/GT in the sense that ChemCam only detected Cu in coherent bedrock not in rubbly. Why is this distinction so strict? We suggest that the Cu abundances are much larger in coherent than in rubbly bedrock owing to very

different geochemical and diagenetic processes in their evolution (cf., Figure 9). This difference is not easily explained in the framework of the lacustrine-groundwater mixing model. The spatial proximity of both bedrock facies in Jm/GT and their sharp contrast in terms of chemical composition (including Cu abundances) may indicate that the location of the lacustrine-groundwater mixing zone moved somewhat over time or that other parameters than the distance to that mixing zone controlled the alteration of the bedrock.

The scenario described so far used Cu, Fe, and Mn abundances in order to characterize the properties (mostly pH) of diagenetic fluids that may have affected rubbly and coherent bedrock. We have shown the success and the limitations of that scenario, which from hereon may be referred to as the "diagenetic model" for Jm/GT and KHm bedrock.

However, the differences in Cu, Fe, and Mn detections between rubbly and coherent bedrock could alternatively be explained by differences in the composition of their respective source regions. This alternative view will be referred to as the "provenance model". Indeed, based on the relative proportions of igneous minerals detected by CheMin (e.g., Rampe et al., 2017; Schieber et al., 2022) or on compositional trends based on ChemCam data (e.g., Bedford, Bridges, et al., 2019), there is considerable evidence that multiple source regions existed for Murray and Carolyn Shoemaker sediments. After all, the rubbly bedrock in Jm/GT is the continuation of the lacustrine Murray sediments below the VRR, where very few Cu detections have been made according to Figure 2. Therefore, it would seem plausible to assume that rubbly bedrock already from the beginning had a very low Cu concentration. The coherent bedrock, on the other hand, would correspond to fluvial sediments and would bear the geochemical signature of a more spatially restricted source region, which was relatively Cu-rich. With this explanation, there would be no need for stronger or additional alteration of the rubbly bedrock, which is not supported by the similarity of CIA values for both types of bedrock (Dehouck et al., 2022) and is difficult to reconcile with the smaller grain size and thus lower permeability of rubbly bedrock as compared to coherent bedrock. In summary, both the "diagenetic model" and the "provenance model" must be considered to explain the difference between rubbly and coherent bedrock in the Jm and KHm members. These are end member models and a combination of these models will also be a valid approach.

A geochemical anomaly was discovered in Outcrops A and B (see previous section, Figure S5 in Supporting Information S1): These two outcrops represent coherent bedrock and are located within a few meters from each other. A striking geochemical difference between the southeastern part of Outcrop A (Ayton/Groken) and Outcrop B (specifically the DS) was their enrichment in Mn/P and Fe/Cu, respectively (Gasda et al., 2022). We see no other possibility than invoking a Cu- and Fe-bearing fluid that would have encountered a pH gradient at the location of Outcrop B to precipitate both Cu and Fe in the DS bedrock. The hypothesized path is shown by a black arrow in Figure 9. There are two possibilities for Cu enrichment in the DS bedrock (Figure 9): (a) by adsorption of Cu^{2+} to newly precipitated ferric hydroxide, or (b) by coprecipitation of this ferric hydroxide and a Cu-bearing solid phase (possibly an oxide). Ferric oxides and hydroxides have only a moderately strong affinity to Cu, with their affinity being weaker than those of manganese oxides and organic matter (Section 2 in this manuscript; Bradl, 2004; Ure & Berrow, 1982). Therefore, we do not favor either one of these two processes and in particular, we do not favor process (a), that is, the adsorption of Cu on a precipitated solid, as we did in the case of the Dillinger member. Both processes involve the oxidation of ferrous iron and subsequent precipitation of amorphous ferric hydroxides. This is consistent with the observation that the DS bedrock is more oxidized (Figure 8). We mentioned earlier that DS bedrock is enriched in iron by several weight percent FeOT, as compared to the average bedrock in the KHm (Figure 7). Based on the above discussion, we suggest that this additional amount of FeOT was initially precipitated as amorphous ferric hydroxide, became crystalline over geologic time and is now present as a crystalline iron oxide (most likely hematite).

As mentioned earlier, Cu detections were strongest in terms of ppm abundances and in terms of spatial confinement in Jm/GT and became significantly weaker in the KHm member. Indeed, we cannot rule out that coherent bedrock at different stratigraphic levels may have inherited different concentrations of Cu from their respective source regions. Alternatively, coherent bedrock may have experienced some limited alteration by acidic fluids, and the occurrence of such sporadic events would have increased up section. The latter model would be consistent with the observation of one such event at Outcrop B and the DS (Figure 9).

6. Conclusions

In this study, we described Cu abundances as measured by ChemCam along Curiosity's traverse. Up to Sol 3007, we identified 10 Cu enhancements. One of these areas of Cu enhancement, that is, the Kimberley area, was already

studied in detail by Payré et al. (2019). Additional Cu enhancements were found in coherent bedrock in the Jm and KHm members in GT. Enrichments in Cu are estimated to be in the range 200–400 ppm, while the Cu background level is likely around 20 ppm or even lower. Most Cu enrichments have been observed in bedrock, but in a number of cases, Cu was found above the background level in diagenetic features (including Ca sulfate veins) as well as in float rocks, such as Gretna Green, which was postulated to be a chondritic meteorite by Lasue et al. (2020).

Based on a pE-pH diagram for the elements Fe, Mn, and Cu, we provided evidence for Cu mobility and two types of bedrock alteration by diagenetic fluids:

1. adsorption of Cu on precipitated Mn oxides (e.g., fracture fills in the Dillinger member at Kimberley),
2. adsorption of Cu on precipitated ferric hydroxides and/or the coprecipitation of ferric hydroxides and Cu-bearing minerals (e.g., DS in GT).

In both cases, the initially precipitated material may have been amorphous/nonstoichiometric and would have evolved partly into crystalline material over time. We favor the interpretation that both processes occurred in situ and post lithification due to the Cu enhancements observed in fracture fills and on narrow patches of bedrock (with strong geochemical gradients on a meter scale) for processes 1 and 2, respectively.

ChemCam Cu data also provided constraints on the nature and evolution of rubbly and coherent bedrock in the Jm and KHm members of GT. Using a lacustrine-groundwater mixing model developed by Thorpe et al. (2022), we hypothesized that rubbly bedrock may have been depleted in Cu and Mn by slightly acidic, shallow-subsurface lake water, while coherent bedrock may have been mostly affected by alkaline groundwater that would not mobilize these elements. However, despite an overall consistency with the lacustrine-groundwater mixing model, we cannot rule out the effects of varying provenance that have been demonstrated for both Murray and Carolyn Shoemaker bedrock (Bedford, Bridges, et al., 2019; Caravaca et al., 2022; Dehouck et al., 2022; Mangold et al., 2019; Rampe et al., 2017; Schieber et al., 2022).

The Cu detections made in the KHm (and also in the Gm) were significantly weaker than those in the Jm. In particular, no Cu (above ChemCam's detection limit of ∼50 ppm) was detected in the two Knockfarril Hill outcrops GE and MA that were heavily studied by the rover. However, the Cu enhancement in the DS demonstrated the local action of acidic fluids in the near vicinity of the MA outcrop. These types of acidic fluids, if occurring on a larger scale, may explain the reduced Cu abundances observed in the KHm.

Following Payré et al. (2019), we favor the idea that Cu enrichments as documented by ChemCam are due to the delivery of clastic material from some Cu-rich source area in (or beyond) the northern rim of Gale crater. Therefore, we consider the above-discussed precipitation of Cu-rich Mn oxides and Fe hydroxides to be examples of local redistribution of Cu that has originally been delivered in the form of Cu-rich clastic material. One of these Cu enhancements, that is, the one at the highest stratigraphic level, was found in the eolian Stimson bedrock, where two (out of 233) ChemCam points turned out to be enriched in Cu and Si. The continued exploration of Mt. Sharp (beyond Sol 3007) may return further ChemCam-Cu data of that bedrock. If Cu enrichment is confirmed in that bedrock at a statistically significant level, then Cu-bearing Stimson sandstone can be compared to Cu-bearing Bradbury group sediments, since both types of sediments apparently share a similar basaltic source region (Bedford et al., 2020).

In conclusion, we tracked Cu abundances along the rover traverse in the sol range from 0 to 3007 and identified different modes of Cu enrichment and redistribution. Building on Payré et al. (2019), we reanalyzed Cu enrichment in the Kimberley area (crater floor). Another focus of this work was the analysis of Cu enrichment in GT, some 300 m above Kimberley, where we used ChemCam Cu data to constrain the evolution of rubbly and coherent bedrock in the Jm and KHm. The predictions on the pH range of fluids that might have affected these types of bedrock were found to be well in line with predictions by Thorpe et al. (2022) that were made in the context of their lacustrine-groundwater mixing model.

Data Availability Statement

Reduced Data Records (RDR) for ChemCam data (including LIBS spectra and derived major-element oxide compositions) used in this article are available through the NASA Planetary Data System (Wiens et al., 2013). Figures 6 and 7 in the present article are directly based on the point-by-point classification of Glen Torridon ChemCam data (Dehouck et al., 2022, Supporting Information Table S1).

Acknowledgments
This work was supported in Germany by Deutsche Forschungsgemeinschaft (DFG-GO 2288/2-1); in the US by the NASA Mars Exploration Program, which supports ChemCam and the Curiosity rover; and in France by CNES and CNRS. Mastcam mosaics (Figures 6a and 7a) were processed by the Mastcam team at Malin Space Science Systems. Jeffrey F. Schroeder, NASA-JPL, provided advice on the elevation data of the rover and nearby targets. Mathias Oehlke, BGU Northeim, provided detailed comments on the manuscript. The review work by Kathryn M. Stack (Jet Propulsion Laboratory, Pasadena) and Jung-Woo Park (Seoul National University) as well as Bradley Thomson, editor of this journal, has been fundamental for this manuscript and is gratefully acknowledged. Open Access funding enabled and organized by Projekt DEAL.

References

Alexander, P. O., & Thomas, H. (2011). Copper in Deccan Basalts (India): Review of the abundance and patterns of distribution. *Boletin del Instituto de Fisiografia y Geologia*, *79–81*, 107–112.

Audetat, A., Zhang, L., & Ni, H. (2018). Copper and Li diffusion in plagioclase, pyroxenes, olivine and apatite, and consequences for the composition of melt inclusions. *Geochimica et Cosmochimica Acta*, *243*, 99–115. https://doi.org/10.1016/j.gca.2018.09.016

Banham, S. G., Gupta, S., Rubin, D. M., Bedford, C. C., Edgar, L. A., Bryk, A. B., et al. (2022). Evidence for fluctuating wind in shaping an ancient Martian dune field: The Stimson formation at the Greenheugh pediment, Gale crater. *Journal of Geophysical Research: Planets*, *127*(9), e2021JE007023. https://doi.org/10.1029/2021JE007023

Banham, S. G., Gupta, S., Rubin, D. M., Edgett, K. S., Barnes, R., Van Beek, J., et al. (2021). A rock record of complex aeolian bedforms in a Hesperian Desert landscape: The Stimson formation as exposed in the Murray buttes, Gale crater, Mars. *Journal of Geophysical Research: Planets*, *126*(4), e2020JE006554. https://doi.org/10.1029/2020JE006554

Banham, S. G., Gupta, S., Rubin, D. M., Watkins, J. A., Sumner, D. Y., Edgett, K. S., et al. (2018). Ancient Martian aeolian processes and palaeomorphology reconstructed from the Stimson formation on the lower slope of Aeolis Mons, Gale crater, Mars. *Sedimentology*, *65*(4), 993–1042. https://doi.org/10.1111/sed.12469

Bedford, C. C., Banham, S. G., Bridges, J. C., Forni, O., Cousin, A., Bowden, D., et al. (2022). An insight into ancient aeolian processes and post-Noachian aqueous alteration in Gale crater, Mars, using ChemCam geochemical data from the Greenheugh capping unit. *Journal of Geophysical Research: Planets*, *127*(9), e2021JE007100. https://doi.org/10.1029/2021JE007100

Bedford, C. C., Bridges, J., Schwenzer, S., Wiens, R., Rampe, E., Frydenvang, J., & Gasda, P. (2019). Alteration trends and geochemical source region characteristics preserved in the fluviolacustrine sedimentary record of Gale crater, Mars. *Geochimica et Cosmochimica Acta*, *246*, 234–266. https://doi.org/10.1016/j.gca.2018.11.031

Bedford, C. C., Schwenzer, S. P., Bridges, J. C., Banham, S., Wiens, R. C., Frydenvang, J., et al. (2019). Using ChemCam-derived geochemistry to identify the paleonet sediment transport direction and source region characteristics of the Stimson formation in Gale crater, Mars. In *#1978, 50th LPSC*. Retrieved from https://www.hou.usra.edu/meetings/lpsc2019/pdf/1978.pdf

Bedford, C. C., Schwenzer, S. P., Bridges, J. C., Banham, S., Wiens, R. C., Gasnault, O., et al. (2020). Geochemical variation in the Stimson formation of Gale crater: Provenance, mineral sorting, and a comparison with modern Martian dunes. *Icarus*, *341*, 113622. https://doi.org/10.1016/j.icarus.2020.113622

Bennett, K. A., Fox, V. K., Bryk, A., Dietrich, W., Fedo, C., Edgar, L., et al. (2022). The Curiosity rover's exploration of Glen Torridon, Gale crater, Mars: An overview of the campaign and scientific results. *Journal of Geophysical Research: Planets*, *127*(1), e2022JE007185. https://doi.org/10.1029/2022JE007185

Beverskog, B., & Puigdomenech, I. (1995). Revised Pourbaix diagrams for copper at 5–150°C (Swedish Nuclear Powel Inspectorate SKI Report 95:73). Retrieved from https://inis.iaea.org/collection/NCLCollectionStore/_Public/27/021/27021617.pdf?r=1%26r=1

Beverskog, B., & Puigdomenech, I. (1997). Revised Pourbaix diagrams for copper at 25 to 300°C. *Journal of the Electrochemical Society*, *144*(10), 3476–3483. https://doi.org/10.1149/1.1838036

Bradl, H. B. (2004). Adsorption of heavy metal ions on soils and soils constituents. *Journal of Colloid and Interface Science*, *277*, 1–18. https://doi.org/10.1016/j.jcis.2004.04.005

Bristow, T. F., Bish, D. L., Vaniman, D. T., Morris, R. V., Blake, D. F., Grotzinger, J. P., et al. (2015). The origin and implications of clay minerals from Yellowknife Bay, Gale crater, Mars. *American Mineralogist*, *100*(4), 824–836. https://doi.org/10.2138/am-2015-5077CCBYNCND

Bristow, T. F., Haberle, R. M., Blake, D. F., Des Marais, D. J., Eigenbrode, J. L., Fairen, A. G., et al. (2017). Low Hesperian PCO_2 constrained from in situ mineralogical analysis at Gale crater, Mars. *Proceedings of the National Academy of Sciences*, *114*(9), 2166–2170. https://doi.org/10.1073/pnas.1616649114

Bristow, T. F., Rampe, E. B., Achilles, C. N., Blake, D. F., Chipera, S. J., Craig, P., et al. (2018). Clay mineral diversity and abundance in sedimentary rocks of Gale crater, Mars. *Science Advances*, *4*(6). eaar3330. https://doi.org/10.1126/sciadv.aar3330

Brückner, J., Dreibus, G., Jagoutz, E., Gellert, R., Lugmair, G., Rieder, R., et al. (2005). Hematite on the surface of Meridiani Planum and Gusev crater. In *LPSC, #1767*. Retrieved from http://www.lpi.usra.edu/meetings/lpsc2005/pdf/1767.pdf

Caravaca, G., Mangold, N., Dehouck, E., Schieber, J., Zaugg, L., Bryk, A. B., et al. (2022). From lake to river: Documenting an environmental transition across the Jura/Knockfarril Hill members boundary in the Glen Torridon region of Gale crater (Mars). *Journal of Geophysical Research: Planets*, *127*(9), e2021JE007093. https://doi.org/10.1029/2021JE007093

Clark, B. C., III, Arvidson, R. E., Gellert, R., Morris, R. V., Ming, D. W., Richter, L., et al. (2007). Evidence for montmorillonite or its compositional equivalent in Columbia Hills, Mars. *Journal of Geophysical Research*, *112*(E6), E06S01. https://doi.org/10.1029/2006JE002756

Clark, B. C., Kolb, V. M., Steele, A., House, C. H., Lanza, N. L., Gasda, P. J., et al. (2021). Origin of life on Mars: Suitability and opportunities. *Life*, *11*(6), 539. https://doi.org/10.3390/life11060539

Clegg, S. M., Wiens, R. C., Anderson, R. B., Forni, O., Frydenvang, J., Lasue, J., et al. (2017). Recalibration of the Mars Science Laboratory ChemCam instrument with an expanded geochemical database. *Spectrochimica Acta B*, *129*, 64–85. https://doi.org/10.1016/j.sab.2016.12.003

Core, D. P., Kesler, S. E., Essene, E. J., Dufresne, E. B., Clarke, R., Arms, D. A., et al. (2005). Copper and zinc in silicate and oxide minerals in igneous rocks from the Bingham – Park City Belt, Utah: Synchrotron X-ray-fluorescence data. *The Canadian Mineralogist*, *43*(5), 1781–1796. https://doi.org/10.2113/gscanmin.43.5.1781

David, G., Cousin, A., Forni, O., Meslin, P.-Y., Dehouck, E., Mangold, N., et al. (2020). Analyses of high-iron sedimentary bedrock and diagenetic features observed with ChemCam at Vera Rubin Ridge, Gale crater, Mars: Calibration and characterization. *Journal of Geophysical Research: Planets*, *125*(10), e2019JE006314. https://doi.org/10.1029/2019JE006314

Dehouck, E., Cousin, A., Mangold, N., Frydenvang, J., Gasnault, O., Forni, O., et al. (2022). Bedrock geochemistry and alteration history of the clay-bearing Glen Torridon region of Gale crater, Mars. *Journal of Geophysical Research: Planets*, *127*(12), e2021JE007103. https://doi.org/10.1029/2021JE007103

Fabre, C., Cousin, A., Wiens, R. C., Ollila, A., Gasnault, O., Maurice, S., et al. (2014). In situ calibration using univariate analyses based on the onboard ChemCam targets: First prediction of Martian rock and soil compositions. *Spectrochimica Acta, Part B*, *99*, 34–51. https://doi.org/10.1016/j.sab.2014.03.014

Fedo, C. M., Bryk, A. B., Edgar, L. A., Bennett, K. A., Fox, V. K., Dietrich, W. E., et al. (2022). Geology and stratigraphic correlation of the Murray and Carolyn Shoemaker formations across the Glen Torridon region, Gale crater, Mars. *Journal of Geophysical Research: Planets*, *127*(9), e2022JE007408. https://doi.org/10.1029/2022JE007408

Ferus, M., Kubelik, P., Knizek, A., Pastorek, A., Sutherland, J., & Civis, S. (2017). High energy radical chemistry formation of HCN-rich atmospheres on early Earth. *Scientific Reports*, *7*(1), 6275. https://doi.org/10.1038/s41598-017-06489-1

Gasda, P. J., Anderson, R. B., Cousin, A., Forni, O., Clegg, S. M., Ollila, A., et al. (2021). Quantification of manganese for ChemCam Mars and laboratory spectra using a multivariate model. *Spectrochimica Acta Part B: Atomic Spectroscopy*, *181*, 106223. https://doi.org/10.1016/j.sab.2021.106223

Gasda, P. J., Comellas, J., Essunfeld, A., Das, D., Bryk, A. B., Dehouck, E., et al. (2022). Overview of the morphology and chemistry of diagenetic features in the clay-rich Glen Torridon unit of Gale crater, Mars. *Journal of Geophysical Research: Planets*, *127*(12), e2021JE007097. https://doi.org/10.1029/2021JE007097

Gasda, P. J., Haldeman, E. B., Wiens, R. C., Rapin, W., ThomasBristow, F., Bridges, J. C., et al. (2017). In situ detection of boron by ChemCam on Mars. *Geophysical Research Letters*, *44*(17), 8739–8748. https://doi.org/10.1002/2017GL074480

Gellert, R. (2013). *Mars science Laboratory Alpha Particle X-ray spectrometer RDR data V1.0* (MSL-M-APXS-4/5-RDR-V1.0). NASA Planetary Data System. https://doi.org/10.17189/1519440

Gellert, R., Boyd, N., Campbell, J. L., VanBommel, S., Thompson, L. M., Schmidt, M. E., et al. (2014). APXS chemical composition of the Kimberley sandstone in Gale crater. *AGU Fall Meeting*, abstract #P34A-05. Retrieved from https://agu.confex.com/agu/fm14/meetingapp.cgi/Paper/11362

Goetz, W., Payre, V., Wiens, R. C., Clegg, S. M., Gasnault, O., Gellert, R., et al. (2018). Detection of copper by the ChemCam instrument onboard the Curiosity rover and search for copper-hosting minerals in Gale crater, Mars. In *#2679, 49th LPSC*. Retrieved from https://www.hou.usra.edu/meetings/lpsc2018/pdf/2679.pdf

Goetz, W., Payre, V., Wiens, R. C., Clegg, S. M., Gasnault, O., Newsom, H., et al. (2019). Detection of copper in Gale crater, Mars, by the ChemCam instrument onboard the Curiosity rover. In *#2848, 50th LPSC*. Retrieved from https://www.hou.usra.edu/meetings/lpsc2019/pdf/2848.pdf

Goetz, W., Payre, V., Wiens, R. C., Gasnault, O., Gellert, R., Newsom, H., et al. (2016). Strong enrichment in copper in the Kimberley area, Gale crater, Mars. In *#2942, 47th LPSC*. Retrieved from http://www.hou.usra.edu/meetings/lpsc2016/pdf/2942.pdf

Goetz, W., Payre, V., Wiens, R. C., Gasnault, O., Gellert, R., Newsom, H., et al. (2017). Detection of copper by the ChemCam instrument along the traverse of the Curiosity rover, Gale crater, Mars. In *#2894, 48th LPSC*. Retrieved from https://www.hou.usra.edu/meetings/lpsc2017/pdf/2894.pdf

Goetz, W., Wiens, R. C., Dehouck, E., Gasnault, O., Lasue, J., Payré, V., et al. (2020). Tracking of copper by the ChemCam instrument in Gale crater, Mars: Elevated abundances in Glen Torridon. In *#2974, 51th LPSC*. Retrieved from https://www.hou.usra.edu/meetings/lpsc2020/pdf/2974.pdf

Grotzinger, J. P., Gupta, S., Malin, M. C., Rubin, D. M., Schieber, J., Siebach, K., et al. (2015). Deposition, exhumation, and paleoclimate of an ancient lake deposit, Gale crater, Mars. *Science*, *350*(6257), aac7575. https://doi.org/10.1126/science.aac7575

Grotzinger, J. P., Sumner, D. Y., Kah, L. C., Stack, K., Gupta, S., Edgar, L., et al. (2014). A habitable fluvio-lacustrine environment at Yellowknife Bay, Gale crater, Mars. *Science*, *343*(6169), 1242777. https://doi.org/10.1126/science.1242777

Halter, W. E., Heinrich, C. A., & Pettke, T. (2005). Magma evolution and the formation of porphyry Cu-Au ore fluids: Evidence from silicate and sulfide melt inclusions. *Mineralium Deposita*, *39*(8), 845–863. https://doi.org/10.1007/s00126-004-0457-5

Jenner, F. E., O'Neill, H. S. C., Arculus, R. J., & Mavrogenes, J. A. (2010). The magnetite crisis in the evolution of arc-related magmas and the initial concentration of Au, Ag and Cu. *Journal of Petrology*, *51*(12), 2445–2464. https://doi.org/10.1093/petrology/egq063

Johnson, J. R., Bell, J., Bender, S., Blaney, D., Cloutis, E., DeFlores, L., et al. (2015). ChemCam passive reflectance spectroscopy of surface materials at the Curiosity landing site, Mars. *Icarus*, *249*, 74–92. https://doi.org/10.1016/j.icarus.2014.02.028

Kramida, A., & Ralchenko, Y. (1999). NIST atomic spectra database, NIST standard reference database 78 [Dataset]. National Institute of Standards and Technology. https://doi.org/10.18434/T4W30F

Lanza, N. L., Wiens, R. C., Arvidson, R. E., Clark, B. C., Fischer, W. W., Gellert, R., et al. (2016). Oxidation of manganese in an ancient aquifer, Kimberley formation, Gale crater, Mars. *Geophysical Research Letters*, *43*(14), 7398–7407. https://doi.org/10.1002/2016GL069109

Lasue, J., Meslin, P. Y., Cohen, B. A., Sautter, V., Bridges, J. C., Lewin, E., et al. (2020). Gretna Green, a possible chondrite detected at Glen Torridon in Gale crater. In *#2125, 51th LPSC*. Retrieved from https://www.hou.usra.edu/meetings/lpsc2020/pdf/2125.pdf

Le Mouélic, S., Gasnault, O., Herkenhoff, K., Bridges, N., Langevin, Y., Mangold, N., et al. (2015). The ChemCam remote micro-imager at Gale crater: Review of the first year of operations on Mars. *Icarus*, *249*, 93–107. https://doi.org/10.1016/j.icarus.2014.05.030

Lodders, K., & Fegley, B., Jr. (1997). An oxygen isotope model for the composition of Mars. *Icarus*, *126*(2), 373–394. https://doi.org/10.1006/icar.1996.5653

Mangold, N., Dehouck, E., Fedo, C., Forni, O., Achilles, C., Bristow, T., et al. (2019). Chemical alteration of fine-grained sedimentary rocks at Gale crater. *Icarus*, *321*, 619–631. https://doi.org/10.1016/j.icarus.2018.11.004

Maurice, S., Wiens, R. C., Saccoccio, M., Barraclough, B., Gasnault, O., Forni, O., et al. (2012). The ChemCam instrument suite on the Mars Science Laboratory (MSL) rover: Science objectives and mast unit description. *Space Science Reviews*, *170*(1–4), 95–166. https://doi.org/10.1007/s11214-012-9912-2

McLennan, S. M., Anderson, R. B., Bell, J. F., Bridges, J. C., Calef, F., Campbell, J. L., et al. (2014). Elemental geochemistry of sedimentary rocks at Yellowknife Bay, Gale crater, Mars. *Science*, *343*(6169), 1244734. https://doi.org/10.1126/science.1244734

Nesbitt, H. W., & Young, G. M. (1982). Early Proterozoic climates and plate motions inferred from major element chemistry of lutites. *Nature*, *299*(5885), 715–717. https://doi.org/10.1038/299715a0

O'Connell-Cooper, C. D., Thompson, L. M., Gellert, R., Spray, J. G., Berger, J. A., Boyd, N. I., et al. (2020). APXS analysis of the Jura and Knockfarril Hill members of the Murray formation within the Glen Torridon locale, Gale crater, Mars. In *#2948, 51th LPSC*. Retrieved from http://www.hou.usra.edu/meetings/lpsc2020/pdf/2948.pdf

Ollila, A. M., Newsom, H. E., Clark, B., Wiens, R. C., Cousin, A., Blank, J. G., et al. (2014). Trace element geochemistry (Li, Ba, Sr, and Rb) using Curiosity's ChemCam: Early results for Gale crater from Bradbury landing site to rocknest. *Journal of Geophysical Research: Planets*, *119*(1), 255–285. https://doi.org/10.1002/2013JE004517

Park, J. W., Campbell, I. H., Ickert, R. B., & Allen, C. M. (2013). Chalcophile element geochemistry of the Boggy Plain zoned pluton, southeastern Australia: A S-saturated barren compositionally diverse magmatic system. *Contributions to Mineralogy and Petrology*, *165*(2), 217–236. https://doi.org/10.1007/s00410-012-0806-9

Park, J. W., Campbell, I. H., Kim, J., & Moon, J. W. (2015). The role of late sulfide saturation in the formation of a Cu- and Au-rich magma: Insights from the platinum Group element Geochemistry of Niuatahi–Motutahi lavas, Tonga rear arc. *Journal of Petrology*, *56*(1), 59–81. https://doi.org/10.1093/petrology/egu071

Patel, B. H., Percivalle, C., Ritson, D. J., Duffy, C. D., & Sutherland, J. D. (2015). Common origins of RNA, protein and lipid precursors in a cyanosulfidic protometabolism. *Nature Chemistry*, *7*(4), 301–307. https://doi.org/10.1038/nchem.2202

Payré, V., Fabre, C., Cousin, A., Sautter, V., Wiens, R. C., Forni, O., et al. (2017). Alkali trace elements in Gale crater, Mars, with ChemCam: Calibration update and geological implications. *Journal of Geophysical Research: Planets*, *122*(3), 650–679. https://doi.org/10.1002/2016JE005201

Payré, V., Fabre, C., Sautter, V., Cousin, A., Mangold, N., Le Deit, L., et al. (2019). Copper enrichments in the Kimberley formation in Gale crater, Mars: Evidence for a Cu deposit at the source. *Icarus*, *321*, 736–751. https://doi.org/10.1016/j.icarus.2018.12.015

Pohl, W. L. (2011). *Economic geology principles and practice: Metals, minerals, coal and Hydrocarbons – Introduction to formation and sustainable exploitation of mineral deposits*. Wiley-Blackwell Publishing Ltd.

Rampe, E. B., Ming, D., Blake, D., Bristow, T., Chipera, S., Grotzinger, J., et al. (2017). Mineralogy of an ancient lacustrine mudstone succession from the Murray formation, Gale crater, Mars. *Earth and Planetary Science Letters*, *471*, 172–185. https://doi.org/10.1016/j.epsl.2017.04.021

Rice, M. S., Gupta, S., Treiman, A. H., Stack, K. M., Calef, F., Edgar, L. A., et al. (2017). Geologic overview of the Mars Science Laboratory rover mission at the Kimberley, Gale crater, Mars. *Journal of Geophysical Research: Planets*, *122*(1), 2–20. https://doi.org/10.1002/2016JE005200

Sasselov, D. D., Grotzinger, J. P., & Sutherland, J. D. (2020). The origin of life as a planetary phenomenon. *Science Advances*, *6*, eaax3419. https://doi.org/10.1126/sciadv.aax3419

Schieber, J., Bohacs, K. M., Coleman, M., Bish, D., Reed, M. H., Thompson, L., et al. (2022). Mars is a mirror – Understanding the Pahrump Hills mudstones from a perspective of Earth analogues. *Sedimentology*, *69*(6), 2371–2435. https://doi.org/10.1111/sed.13024

Stern, J. C., Navarro-González, R., Freissinet, C., Mckay, C. P., Archer, P. D., Buch, A., et al. (2014). Detection and quantification of nitrogen compounds in the first drilled Martian solid samples by the Sample Analysis at Mars (SAM) instrument suite on the Mars Science Laboratory (MSL). In *45th LPSC, #2743*. Retrieved from https://www.hou.usra.edu/meetings/lpsc2014/pdf/2743.pdf

Stern, J. C., Sutter, B., Freissinet, C., Navarro-González, R., McKay, C. P., Archer, P. D., Jr., et al. (2015). Evidence for indigenous nitrogen in sedimentary and aeolian deposits from the Curiosity rover investigations at Gale crater, Mars. *Proceedings of the National Academy of Sciences*, *112*(14), 4245–4250. Retrieved from https://www.pnas.org/content/112/14/4245

Stolper, E. M., Baker, M. B., Newcombe, M. E., Schmidt, M. E., Treiman, A. H., Cousin, A., et al. (2013). The petrochemistry of Jake_M: A Martian mugearite. *Science*, *341*(6153). https://doi.org/10.1126/science.1239463

Sutherland, J. D. (2015). Origins of life systems chemistry. *EPSC Abstracts*, *10*, EPSC2015-1. Retrieved from https://meetingorganizer.copernicus.org/EPSC2015/EPSC2015-1.pdf

Taylor, G. J. (2013). The bulk composition of Mars. *Geochemistry*, *73*(4), 401–420. https://doi.org/10.1016/j.chemer.2013.09.006

Thorpe, M. T., Bristow, T. F., Rampe, E. B., Tosca, N. J., Grotzinger, J. P., Bennett, K. A., et al. (2022). Mars Science Laboratory CheMin data from the Glen Torridon region and the significance of lake-groundwater interactions in interpreting mineralogy and sedimentary history. *Journal of Geophysical Research: Planets*, *127*(11), e2021JE007099. https://doi.org/10.1029/2021JE007099

Treiman, A. H., Bish, D. L., Vaniman, D. T., Chipera, S. J., Blake, D. F., Ming, D. W., et al. (2016). Mineralogy, provenance, and diagenesis of a potassic basaltic sandstone on Mars: CheMin X-ray diffraction of the Windjana sample (Kimberley area, Gale crater). *Journal of Geophysical Research: Planets*, *121*(1), 75–106. https://doi.org/10.1002/2015JE004932

Udry, A., Howarth, G. H., Herd, C. D. K., Day, J. M. D., Lapen, T. J., & Filiberto, J. (2020). What Martian meteorites reveal about the interior and surface of Mars. *Journal of Geophysical Research: Planets*, *125*(12), e2020JE006523. https://doi.org/10.1029/2020JE006523

Ure, A. M., & Berrow, M. L. (1982). The elemental constituents of soils. In H. J. M. Bowen (Ed.), *Environmental chemistry* (Vol. 2, p. 136). Royal Society of Chemistry.

VanBommel, S. J., Gellert, R., Berger, J., Yen, A., & Boyd, N. (2019). Mars Science Laboratory Alpha Particle X-ray spectrometer trace elements: Situational sensitivity to Co, Ni, Cu, Zn, Ga, Ge, and Br. *Acta Astronautica*, *165*, 32–42. https://doi.org/10.1016/j.actaastro.2019.08.026

Vaniman, D. T., Bish, D. L., Ming, D. W., Bristow, T. F., Morris, R. V., Blake, D. F., et al. (2014). Mineralogy of a mudstone at Yellowknife Bay, Gale crater, Mars. *Science*, *343*(6169), 1243480. https://doi.org/10.1126/science.1243480

Vasavada, A. R. (2022). Mission overview and scientific contributions from the Mars Science Laboratory Curiosity rover after eight years of surface operations. *Space Science Reviews*, *218*(3), 14. https://doi.org/10.1007/s11214-022-00882-7

Wang, Z., & Becker, H. (2017). Chalcophile elements in Martian meteorites indicate low sulfur content in the Martian interior and a volatile element-depleted late veneer. *Earth and Planetary Science Letters*, *463*, 56–68. https://doi.org/10.1016/j.epsl.2017.01.023

Wiens, R. C., Blazon-Brown, A. J., Melikechi, N., Frydenvang, J., Dehouck, E., SamuelClegg, M., et al. (2021). Improving ChemCam LIBS long-distance elemental compositions using empirical abundance trends. *Spectrochimica Acta Part B: Atomic Spectroscopy*, *182*, 106247. https://doi.org/10.1016/j.sab.2021.106247

Wiens, R. C., Maurice, S., Barraclough, B., Saccoccio, M., Barkley, W. C., Bell, J. F., et al. (2012). The ChemCam instrument suite on the Mars Science Laboratory (MSL) rover: Body unit and combined system tests. *Space Science Reviews*, *170*(1–4), 167–227. https://doi.org/10.1007/s11214-012-9902-4

Wiens, R. C., Maurice, S., Lasue, J., Forni, O., Anderson, R. B., Clegg, S., et al. (2013). Pre-flight calibration and initial data processing for the ChemCam laser-induced breakdown spectroscopy instrument on the Mars Science Laboratory rover. *Spectrochimica Acta Part B Atomic Spectroscopy*, *82*, 1–27. https://doi.org/10.1016/j.sab.2013.02.003

Xu, J., Ritson, D. J., Ranjan, S., Todd, Z. R., Sasselov, D. D., & Sutherland, J. D. (2018). Photochemical reductive homologation of hydrogen cyanide using sulfite and ferrocyanide. *Chemical Communications*, *54*(44), 5566–5569. https://doi.org/10.1039/c8cc01499j

Yen, A., Clark, B. C., Ming, D. W., Mittlefehldt, D. W., Gellert, R., & Morris, R. V. (2010). Chemical alteration on Mars indicated by the iron-manganese ratio. In *LPSC, #2546*. Retrieved from http://www.lpi.usra.edu/meetings/lpsc2010/pdf/2546.pdf

Yoshizaki, T., & McDonough, W. F. (2020). The composition of Mars. *Geochimica et Cosmochimica Acta*, *273*, 137–162. https://doi.org/10.1016/j.gca.2020.01.011

References From the Supporting Information

Francis, R., Estlin, T., Gaines, D., Bornstein, B., Schaffer, S., Verma, V., et al. (2015). AEGIS autonomous targeting for the Curiosity rover's ChemCam instrument. In *IEEE Applied Imagery Pattern Recognition Workshop (AIPR)* (pp. 1–5). https://doi.org/10.1109/AIPR.2015.7444544